1   **Observations of creep of polar firn at different temperatures**

2

3   Yuan Li[1,3], Kaitlin Keegan[2], Ian Baker[1]

4   [1]Thayer School of Engineering, Dartmouth College, Hanover, NH, 03755, USA

5   [2]Department of Geological Sciences & Engineering, University of Nevada, Reno, Reno, NV,

6   89557, USA

7   [3]X-Here (Future ice-based Hydrogen energy & resilient environments) Trek Laboratory

8   (Establishing), Howard Beach, NY, 11414, USA

9   *Correspondence to*: Ian Baker (ian.baker@dartmouth.edu)

Abstract

To improve our understanding of firn compaction and deformation processes, constant-load compressive creep tests were performed on specimens from a Summit, Greenland (72°35' N, 38°25' W) firn core that was extracted in June, 2017. Cylindrical specimens were tested at temperatures of –5°C, –18°C and –30°C from depths of 20 m, 40 m and 60 m at stresses of 0.21 MPa, 0.32 MPa and 0.43MPa, respectively. The microstructures were characterized before and after creep using both X-ray micro-computed tomography (micro-CT) and thin sections viewed between optical crossed polarizers. The results of these experiments comprise a novel data set on the creep of firn at three depths of a firn column at three different temperatures, providing useful calibration data for firn model development. Examining the resulting strain vs. time and strain vs. strain rate curves from the creep tests revealed the following notable features. First, the time exponent k was found to be 0.34–0.69 during transient creep, which is greater than the 0.33 usually observed in fully-dense ice. Second, the strain rate minimum (SRmin) in secondary creep occurred at a greater strain from specimens with lower density and at higher temperatures. Third, tertiary creep occurred more easily for the lower-density specimens at greater effective stresses and higher temperatures, where strain softening is primarily due to recrystallization. Fourth, the SRmin is a function of the temperature for a given firn density. Lastly, we developed empirical equations for inferring the SRmin, as it is difficult to measure during creep at low temperatures. The creep behaviors of polar firn, being essentially different from full-density ice, imply that firn densification is an indispensable process within the snow-to-ice transition, particularly firn deformation at different temperatures connected to a changing climate.

32   **Keywords:** Firn densification; Creep; Activation energy; Cryospheric micro-CT; Temperature

1. Introduction

Understanding firn compaction and densification experimentally is critical for developing physics-based firn models that are necessary for many glaciological applications, e.g. reconstructing ice-core paleoclimate records, interpreting ice-mass changes from satellite altimetry data, and even developing clean hydrogen production and storage technology (Li, 2023a; 2024a; 2024b; 2024c). However, the firn models used for these applications are empirical and are known to perform poorly outside of their calibration range (Lundin et al., 2017). Thus, a better understanding of firn compaction is necessary to refine firn models for these important glaciological applications. Laboratory compressive experiments on firn and ice improve our understanding of their respective flow laws and advance the development of firn models under a range of conditions. The rheology of polycrystalline ice, particularly its temperature-dependent creep deformation, is a cornerstone of glaciological modeling. Numerous studies have established a robust framework for understanding ice deformation, primarily through laboratory creep experiments (e.g. Glen, 1955; Weertman, 1983; Budd and Jacka, 1989; Durham et al., 2001; Goldsby and Kohlstedt, 2001; Petrenko and Whitworth, 1999). This body of work has confirmed that ice creep is strongly governed by temperature, typically described by an Arrhenius relationship with a well-constrained activation energy for grain-scale processes like dislocation glide and climb (e.g. Jacka, 1984; Hooke, 2005). In contrast, the mechanical behavior of firn, the intermediate porous material between snow and glacial ice, remains comparatively poorly characterized, especially with respect to temperature. It is important to note that "the experimental observations are discussed with respect to the mechanical properties of polycrystalline ice, which is the constituent material of the load-bearing ice skeleton" (Scapozza and Bartelt, 2003), sharing

55 poromechanics-based deformation mechanisms between the two via continuum mechanics and

56 homogenization framework (Gagliardini and Meyssonnier, 2000; Coussy, 2004; Hutter and Johnk,

57 2004; Srivastava et al., 2010). While numerous studies have investigated firn and ice deformation

58 (e.g. Steinemann, 1954; Landauer, 1958; Mellor, 1975; Salm, 1982; Maeno and Ebinuma, 1983;

59 Ambach and Eisner, 1985; Li et al., 1996; Meussen et al., 1999; Bartelt and von Moos, 2000;

60 Jacka and Li, 2000; Song et al., 2006a, 2006b, 2008; Theile et al., 2011; Treverrow et al., 2012;

61 Hammonds and Baker, 2016, 2018; Li and Baker, 2021, 2022a), existing firn data are sparse and

62 fragmented. A critical knowledge gap persists in the systematic experimental quantification of

63 firn's mechanical response across a broad range of temperatures. Temperature is a first-order

64 control on firn densification and deformation rates, yet most laboratory studies have been

65 conducted at a limited number of isothermal conditions, often focused on a single density or at

66 temperatures near the melting point (e.g. Mellor, 1975; Maeno and Ebinuma, 1983). Consequently,

67 there is a pronounced lack of experimental data necessary to derive the systematic activation

68 energy for the creep of firn over its full density spectrum. This parameter is not merely a scalar

69 but is likely a function of density, microstructure, and the dominant deformation mechanism

70 (compaction versus shear), transitioning from grain-boundary sliding in low-density firn to

71 dislocation creep in high-density firn and ice (Hammonds and Baker, 2018; Li, 2022; Li and

72 Baker, 2022a). The absence of comprehensive, temperature-variable creep data for firn across its

73 density range renders it insufficient for constraining the temperature-dependence terms in modern,

74 physics-based firn models. Our work fills this gap via X-ray micro-computed

75 tomography-analyzed mechanical examinations, e.g. a systematic series of constant-stress creep

76 experiments on firn cores of varying density, conducted across a thermally controlled range from

77 –30°C to –5°C. This allows for the direct determination whether the apparent activation energy is

78 a function of density, thereby providing the essential experimental foundation needed to improve

79 predictions of firn densification in ice-sheet and glacier models. Notably, the mechanical behavior

80 of two-phase flow coupling the airflow with the ice matrix deformation has not yet been

81 performed experimentally hitherto, even though the role of the microstructures of firn on airflow

82 has been studied (Albert et al., 2000; Courville et al., 2010; Adolph and Albert, 2014). This

83 difficulty is largely due to the limitations of the observation techniques of nondestructive

84 visualization of the microstructures during snow and firn deformation. Thus, caution should be

85 taken when extending the conclusions to ice sheet and glacier scales from sample laboratory

86 experiments. Macroscopically, the creep of firn obeys a power-law dependence of the strain rate

87 on the stress at constant stresses and temperature, similar to that of full-density ice (Li and Baker,

88 2022a). Note that both the diffusivity and permeability of the air in the pores (Albert et al., 2000;

89 Courville et al., 2010; Adolph and Albert, 2014) impact heat conduction of the ice matrix, and

90 hence the grain growth. This is tightly tied to the micro-mechanisms, e.g. grain-boundary and

91 lattice diffusion of the ice crystals (Li and Baker, 2021), superplastic deformation and

92 inter-particle sliding from dislocation motion in the ice necks (Bartelt and Von Moos, 2000), and

93 likely rearrangement of the ice particles (Perutz and Seligman, 1939; Anderson and Benson, 1963;

94 Ebinuma and Maeno, 1987).

95

96 Through experiments on isotropic ice samples subjected to uni-axial compaction at octahedral

97 stresses of 0.1–0.8 MPa and temperatures from –45°C to –5°C, Jacka and Li (2000) determined

98 the mechanisms involved in the empirical *power-law flow*, which was derived by Glen (1955) for

99   stresses ranging from 0.1–1 MPa at temperatures spanning from –13ºC to the melting-point. They

100   found that dynamic recrystallization predominated at higher temperatures and stresses, whereas

101   crystal rotation governed at lower temperatures and stresses. Later, Goldsby and Kohstedt (2001)

102   found that ice could exhibit *superplastic flow*, which depends inversely on the grain size,

103   particularly for fine-grained ice, while both dislocation creep and basal slip-limited creep were

104   unrelated to the grain size at stresses of 0.1 MPa or less over a wide range of temperatures.

105   Moreover, Baker and Gerberich (1979) reported that the apparent activation energy for creep for

106   polycrystalline ice, which was derived from tests at constant stress and temperatures ranging from

107   –40ºC to –5ºC, increased with increasing volume fraction of inclusions (bubbles, impurities, dust,

108   and air clathrate hydrates). Such inclusions governed the evolution of grain size related to thermal

109   activations. The activation energies for the creep of snow and ice have been determined by a

110   number of authors, and values ranging from 58.6–113 kJ mol^{-1} were obtained under both uniaxial

111   and hydrostatic experiments for snow with a density of ~400 kg m^{-3} at –13.6ºC to –3.6ºC

112   (Landauer, 1958); 44.8–74.5 kJ mol^{-1} from snow with densities of 440–830 kg m^{-3} at –34.5ºC to –

113   0.5ºC (Mellor and Smith, 1966); ~72.9 kJ mol^{-1} for firn with a density of 320–650 kg m^{-3} at the

114   South Pole (Gow, 1969); 69 ± 5 kJ mol^{-1} for a mean snow density of 423 ± 8 kg m^{-3} at –19ºC to

115   –11ºC (Scapozza and Bartelt, 2003); the 78 kJ mol^{-1} from polycrystalline ice compression

116   deformation at a temperature of –10 ºC (Duval and Ashby, 1983); ~60 kJ mol^{-1} for artificial and

117   natural ice at the South Pole (Pimienta and Duval, 1987); and 78 ± 4 kJ mol^{-1} for monocrystal ice

118   at –20ºC to –4.5ºC and 75 ± 2 kJ mol^{-1} for bicrystal ice at –15ºC to –4.5ºC (Homer and Glen,

119   1978). In summary, the flow law of polycrystalline ice and firn depends on the effects of

120   recrystallization, grain size, inclusions (Mellor and Testa, 1969; Vickers and Greenfield, 1968;

121 Barnes et al., 1971; Baker and Gerberich, 1979; Goodman et al., 1981), and the temperature.

122

123 With advanced observation techniques, the relevant microstructural parameters of snow and firn

124 have been characterized by a number of scientists (Arnaud et al., 1998; Coleou et al., 2001; Flin et

125 al., 2004; Wang and Baker, 2013; Wiese and Schneebeli, 2017; Li, 2022). Using X-ray

126 micro-computed tomography (micro-CT), Li and Baker (2022b) characterized metamorphism

127 from snow to depth hoar under opposing temperature gradients. Only rarely has work been

128 performed on the co-effects of temperature and stress on the densification of firn while

129 simultaneously visualizing the microstructural changes using a micro-CT. For example, Schleef et

130 al. (2014) reported that densification under varying conditions of overburden stress and

131 temperature from natural and laboratory-grown new snow showed a linear relationship between

132 density and the specific surface area (SSA). To this end, the aim of our present work is to

133 investigate the temperature dependence of the creep of polar firn and relate this to the change of

134 microstructure determined using micro-CT studies on firn obtained from Summit, Greenland in

135 2017. As is well known, temperature is a key parameter affecting the flow of firn and ice, and

136 plays a determined role in their deformation, especially for polythermal and temperate glaciers.

137 Due to the great difficulty of analyzing firn and ice deformation with the presence of liquid water,

138 this work focuses on the firn creep from the dry snow zone, i.e., areas without meltwater, at

139 different temperatures.

140

141 **2. Samples and measurements**

142 2.1 *Samples*

143   Three cylindrical samples (22 ± 0.5 mm diameter; 50 ± 0.5 mm high) were produced at each of

144   three depths of 20 m, 40 m and 60 m from the same 2017 Summit, Greenland firn core that was

145   studied in Li and Baker (2022a). Both the densities and porosities of these above samples are

146   typical of values in the snow-to-ice transition zone as introduced in Section 1. It is important to

147   note that the reduction in effective stress with increasing depth is evident in samples taken from

148   these three specified depths (**Appendix A**). Before creep testing, one cylindrical firn samples

149   from each depth was stored at a temperature of –5 ± 0.5°C, –18 ± 0.5°C, and –30 ± 0.5°C for two

150   days to achieve thermal equilibrium (Li and Baker, 2022a). It's also important to note that firn is a

151   heterogeneous material that can have variations in layering, fabric, grain size, and impurity

152   concentration across short distances. Thus, care was taken to extract the three replicate samples

153   from the core at each depth as closely as possible to reduce the variability in their initial

154   conditions.

155

156   *2.2 Creep measurements*

157   Three home-built creep jigs were placed in individual Styrofoam boxes in three different cold

158   rooms that were held at temperatures of –5 ± 0.5°C, –18 ± 0.5°C and –30 ± 0.5°C. Each creep jig

159   consists of an aluminum base plate and three polished aluminum-guide rails passing through

160   linear bearings that hold the upper aluminum loading plate (**Figure 1**). A linear voltage

161   differential transducer (LVDT-Omega LD-320: resolution of 0.025%; linearity error of ± 0.15%

162   of full-scale output), parallel to the three aluminum-guide rails, was located adjacent to the center

163   of the upper plate, and fixed firmly using a screw through the plate (**Figure 1**) for measuring the

164   displacement during a test. The displacement was logged every 5 seconds using a Grant SQ2010

165 datalogger (accuracy of 0.1%). Temperatures were logged at 300-second time intervals over the

166 entire test period, using a k-type thermocouple (Omega RDXL4SD thermistor: resolution of 0.1°C)

167 that was mounted inside each box. In this work, specimens were tested at temperatures of $-5 \pm$

168 0.2°C, $-18 \pm 0.2^{\circ}$C and $-30 \pm 0.2^{\circ}$C from depths of 20 m (applied stress 0.21 MPa), 40 m (0.32

169 MPa) and 60 m (0.43 MPa). There are smaller error bars for the temperature of the specimens

170 than the room temperature because the creep jigs were in insulated Styrofoam boxes. The stresses

171 were chosen based on experience from previous tests (Li and Baker, 2022a) in order to give

172 measurable creep rates in a reasonable time.

173
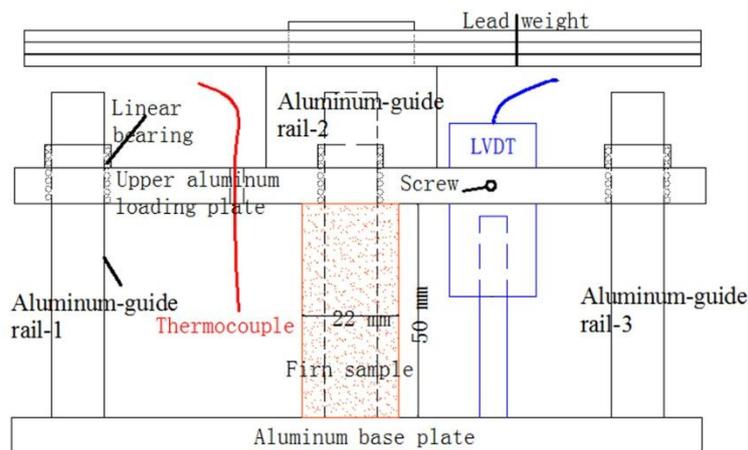
174

175 **Figure 1:** Schematic illustrating the home-built compressive creep jigs. More details can be found

176 in (Li & Baker, 2022a).

177

178

179 2.3 *X-ray micro-computed tomography (micro-CT)*

180 Each specimen at each depth and temperature combination was scanned using a Skyscan 1172

181 micro-CT, before and after creep testing. Each micro-CT scan lasted ~2 h. The cubic Volume of

182   Interest (VOI, a side length of 8 mm) was taken from near the center of the firn specimen as

183   conducted in Li and Baker (2022a). The microstructural parameters obtained from the micro-CT

184   data are the SSA, the mean structure thickness of the ice matrix (S.Th), the area-equivalent circle

185   diameter of the pores (ECDa), the total porosity (TP), the closed porosity (CP), and the structure

186   model index (SMI). The SSA (mm^{-1}) is the ratio of the ice surface area to total firn volume (ice

187   plus air) in a VOI analytical element, and is calculated using the hexahedral marching cubes

188   algorithm via CTAn software (Wang and Baker, 2013). It characterizes the thickness and

189   complexity of the firn microstructure. Changes in SSA indicate a change in free energy of the ice

190   surfaces, the decrease of which represents the occurrence of sintering-pressure. The S.Th (mm) is

191   the mean structure thickness of an ice matrix (Hildebrand and Ruegsegger, 1997), which

192   represents the characteristic size of an ice particle in the firn, where the ice particle consists of one

193   or many crystals or grains. It is measured based on the largest sphere diameter that encloses a

194   point in the ice matrix and is completely bounded within solid surfaces. The ECDa (mm) is the

195   diameter of a circle having the same area as the average for all pores in the VOI from the 2-D

196   binary images, indicative of the characteristic size for the void space (Adolph and Albert, 2014).

197   The TP (%) is the ratio of the pore volume, including both open and closed pores, to the total VOI.

198   The CP (%) is the ratio of the volume of the closed pores to the total volume of solid plus closed

199   pores volume in a VOI, while the open porosity (%) is the ratio of the volume of the open pores to

200   the total VOI. The SMI is calculated based on the dilation of a 3-D voxel model (Hildebrand and

201   Ruegsegger, 1997) $\mathrm{SMI} = 6\left(S' \times V\right)\big/S^{2}$, where S' is the change in the surface area due to

202   dilation, and V and S are the object volume and surface area, respectively. It indicates the

203   prevalent ice curvature, negative values of which represent a concave surface, e.g. the hollow air

204 structure surrounded by an ice matrix. The more negative the SMI value, the more spherical the

205 pore. Notably, the micro-CT-derived density of each specimen agrees well with the bulk density

206 measured using the mass-volume approach (Li and Baker, 2021).

207

208 *2.4 Thin section preparation and imaging*

209 Thin sections for optical photographs before and after creep testing were cut from bulk specimens,

210 one side of which was first smoothed with a microtome. This side was then frozen onto a glass

211 plate ($100 \times 60 \times 2$ mm) by dropping supercooled gas-free water along its edges. Its thickness

212 was reduced to ~2 mm by a band saw, and finally thinned further to a uniform thickness of ~0.5

213 mm using a microtome. Images were captured using a digital camera after each thin section was

214 placed on a light table between a pair of crossed polarizing sheets.

215

216 **3 Results and discussion**

217 3.1 *Microstructures before creep*

218 Increasing firn density with increasing depth from either of the –5°C, –18°C, and –30°C

219 specimens can be readily recognized by visual inspection of the micro-CT 3-D reconstructions of

220 the firn microstructure (**Figure 2**). Correspondingly, the microstructural parameters, with the

221 exception of the CP, changed monotonically with increasing depth at each temperature, e.g. the –

222 30°C samples increased in density from 591 ± 1.4 kg m^{-3}, to 683 ± 4.2 kg m^{-3}, to 782 ± 1.5 kg m^{-3},

223 decreased in SSA from 4.64 ± 0.04 mm^{-1}, to 3.3 ± 0.06 mm^{-1}, to 2.39 ± 0.01 mm^{-1}, and decreased

224 in TP from $35.6 \pm 0.05\%$, $25.6 \pm 0.4\%$, to $14.8 \pm 0.2\%$ at 20, 40, and 60 m, respectively (**Table 1**).

225 These above changes are similar to those previously observed in this firn core (Li and Baker,

226 2022a), implying that the sintering-pressure mechanism plays a crucial role in the densification of

227 polar firn due to the increasing overburden of snow and firn with increasing depth. However, the

228 microstructures of the samples from the three temperatures at each depth show little variability

229 and do not monotonically change with temperature, e.g. at 20 m depth the -5°C, -18°C, and $-$

230 30°C samples having densities of 589 ± 1.3 kg m^{-3}, 615 ± 2.5 kg m^{-3}, and 591 ± 1.4 kg m^{-3}, and

231

	−5ºC	−18ºC	−30ºC

20 m; Before Creep   20 m; Before Creep   20 m; Before Creep

232

20 m; After 12.7% Strain   20 m; After 3.3% Strain   20 m; After 1.2% Strain

233

40 m; Before Creep   40 m; Before Creep   40 m; Before Creep

234

40 m; After 19.3% Strain   40 m; After 4.3% Strain   40 m; After 1.2% Strain

235

60 m; Before Creep   60 m; Before Creep   60 m; Before Creep

236
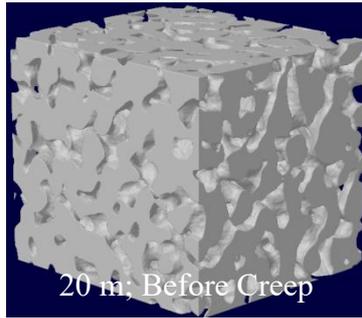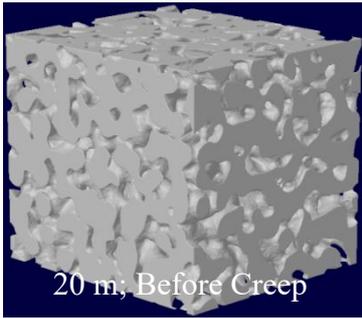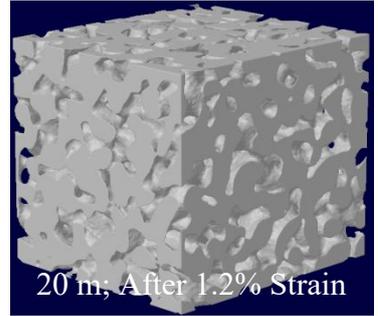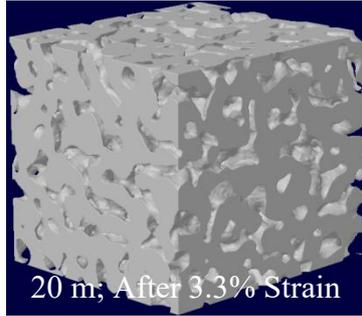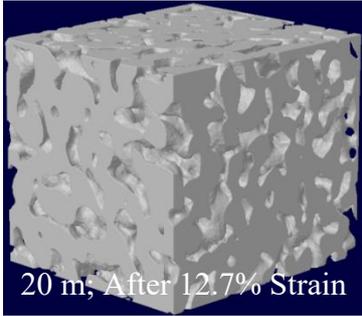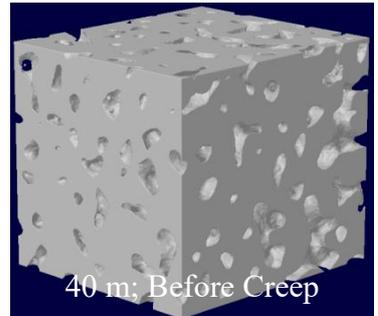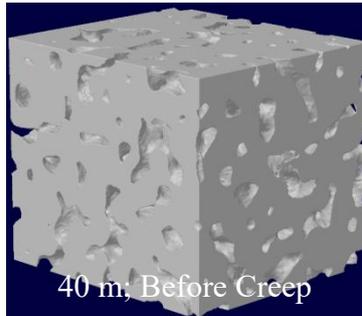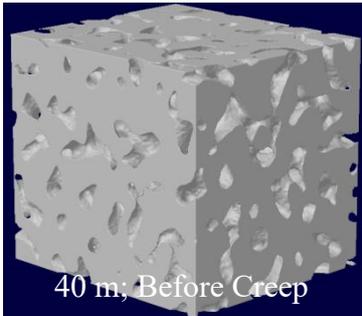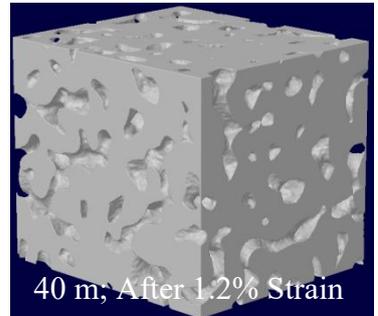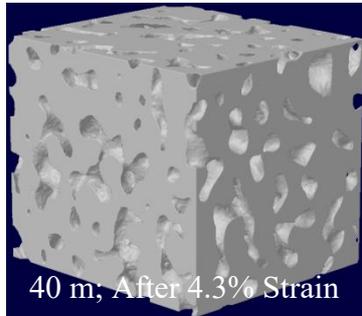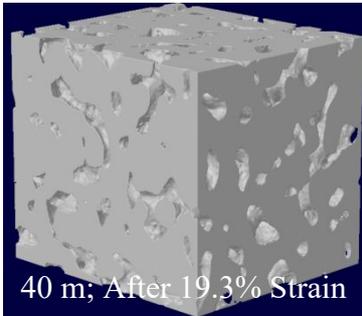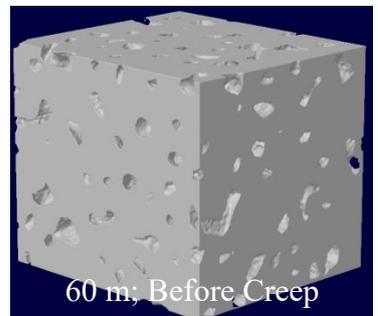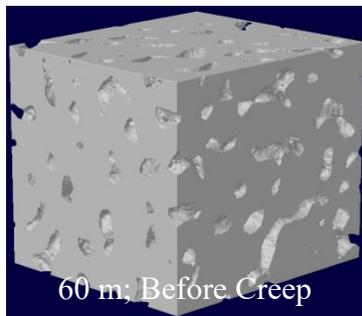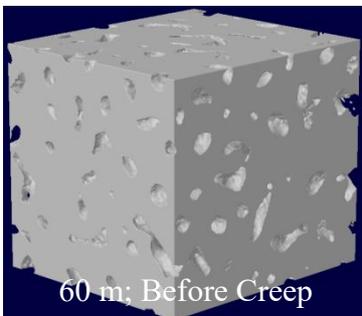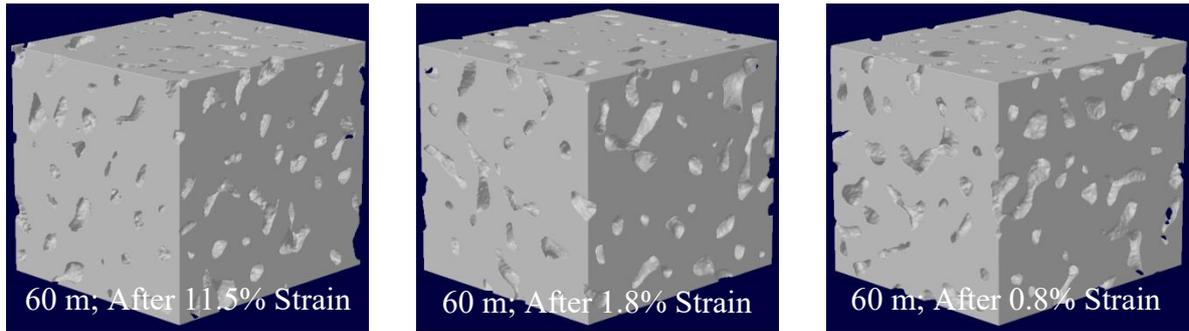
Figure 2: Micro-CT 3-D reconstructions (the side length of each cubic volume of interest is 8 mm) of specimens before and after creep testing at the depths and temperatures shown. Grey voxels represent ice in the firn structure.

Table 1. Microstructural parameters derived from Micro-CT for samples at –5ºC, –18ºC, and –30ºC from depths of 20 m, 40 m, and 60 m before creep.

20m							
T	Density	SSA	S.Th	TP	CP		ECDa
ºC	kg m⁻³	mm⁻¹	mm	%	%	SMI	mm
–5	589±1.3	4.74±0.03	0.732±0.001	35.9±0.08	0.03±0.002	-0.31±0.04	1.07±0.005
–18	615±2.5	4.51±0.04	0.758±0.001	33.1±0.2	0.01±0.001	-0.57±0.01	0.995±0.013
–30	591±1.4	4.64±0.04	0.747±0.004	35.6±0.05	0.02±0.001	-0.27±0.05	1.09±0.004

40m							
T	Density	SSA	S.Th	TP	CP		ECDa
ºC	kg m⁻³	mm⁻¹	mm	%	%	SMI	mm
–5	685±1.4	3.26±0.04	0.95±0.004	25.5±0.1	0.015±0.001	-1.85±0.11	0.857 ±0.005
–18	669±0.6	3.41±0.04	0.914±0.003	27.1±0.03	0.01±0.001	-1.69±0.09	0.892±0.002
–30	683±4.2	3.30±0.06	0.94±0.01	25.6±0.4	0.021±0.005	-1.87±0.13	0.86±0.01

60m							
T	Density	SSA	S.Th	TP	CP		ECDa
ºC	kg m⁻³	mm⁻¹	mm	%	%	SMI	mm
–5	790±1.0	2.34±0.03	1.1±0.003	14.0±0.1	0.11±0.01	-4.81±0.22	0.594±0.003
–18	780±0.5	2.37±0.03	1.08±0.01	15.2±0.06	0.014±0.007	-4.8±0.2	0.632±0.001
–30	782±1.5	2.39±0.01	1.076±0.0003	14.8±0.2	0.02±0.001	-4.92±0.14	0.639±0.002

Note: SSA is the specific surface area, S.Th is the structure thickness, TP is the total porosity, CP

248   is the closed porosity, SMI is the structure model index, and ECDa is the area-equivalent circle

249   diameter.

250

251

252   SSAs of 4.74 ± 0.03 mm^{-1}, 4.51 ± 0.04 mm^{-1}, and 4.64 ± 0.04 mm^{-1}, respectively (**Figures 2–3**;

253   **Table 1**). Here, despite the -18°C specimen having a higher density than the two others at -5°C

254   and -30°C, is not possible to conclude that the sintering of firn is not directly related to the

255   temperature. This is likely because a thermal equilibration period of two days in the absence of

256   compression is too short to sufficiently exert the influence of temperature on firn sintering. The

257   microstructural differences seen in these specimens more likely arose from the initial samples

258   themselves, which were anisotropic and heterogeneous even if taken from the same depth,

259   attributed to firn pre-deformation and partial annealing before experiments (Li and Baker, 2022a).

260

261   3.2 *Microstructures after creep*

262   The microstructural evolution is characterized by the microstructural parameters shown in **Figure**

263   **3**. The largest changes occurred in the -5°C specimens due to the higher temperature, i.e., the

264   density, S.Th, and CP increased, while the ECDa, TP, SSA, and SMI decreased, indicative of

265   consolidation of the firn after creep. It is important to note that for the 60 m sample tested at -5°C,

266   there was no change in density, i.e., 790.2 ± 1 kg m^{-3} before creep vs. 790.7 ± 0.9 kg m^{-3} after

267   creep, or TP, i.e., $14.0 \pm 0.1\%$ before creep vs. $13.9 \pm 0.1\%$ after creep. This lack of

268   microstructural change is due to the high initial density, which was close to the firn pore close-off

269   density of ~830 kg m^{-3}. Thus, the creep of this sample may involve a transition from firn to

270 bubbly ice, as is also indicated by the increase in CP, which would have made it difficult to

271 compress further. Intriguingly, some of the changes in microstructure observed in the micro-CT

272 3-D reconstructions from the specimens before and after creep, e.g. the distribution of ice-space,

273 are indistinguishable in **Figure 2**. This is presumably due to the relatively large initial particle size,

274 or from radial dilation exceeding the axial compression because of the small strains that occurred

275 at relatively low temperatures.

276

277 One exception to the expected microstructural change after creep was the decrease of CP, which

278 was likely due to the measurement uncertainty of the micro-CT (Burr et al., 2018), or radial

279 expansion of the specimen during creep. Another exception was the decrease in density after

280 creep for the $-18\,^{\circ}\mathrm{C}$ specimen at 20 m and the $-30\,^{\circ}\mathrm{C}$ specimen at 60 m, which arose due to a

281 de-densification effect produced by temperature gradient metamorphism, as confirmed by the

282 increase of both TP and S.Th (Li and Baker, 2022b). The thermal gradient appears to be

283 associated with a fluctuation of $0.2\,^{\circ}\mathrm{C}$ around the test temperature, similar to temperature cycling

284 occurred within firn (Mellor and Testa, 1969; Weertman, 1985), which stems from the

285 thermometer's inherent accuracy as noted in Section 2.2 ($-5 \pm 0.2\,^{\circ}\mathrm{C}$, $-18 \pm 0.2\,^{\circ}\mathrm{C}$ and $-30 \pm$

286 $0.2\,^{\circ}\mathrm{C}$). In the relatively simple deformation found at ice-sheet dome sites, such as Summit, there

287 is no mechanism to decrease density during compression. At sites closer to the ice sheet margins,

288 cracking due to extension of the ice may cause a localized decrease in density. The rate of firn

289 densification should decrease with increasing depth at a given temperature, due to the decrease of

290 effective stress with increasing depth (**Appendix A**). As a matter of fact, the density of the $-5\,^{\circ}\mathrm{C}$

291 samples after creep increased by 32 kg m^{-3}, 44 kg m^{-3}, and 0.5 kg m^{-3} for the 20 m, 40

17
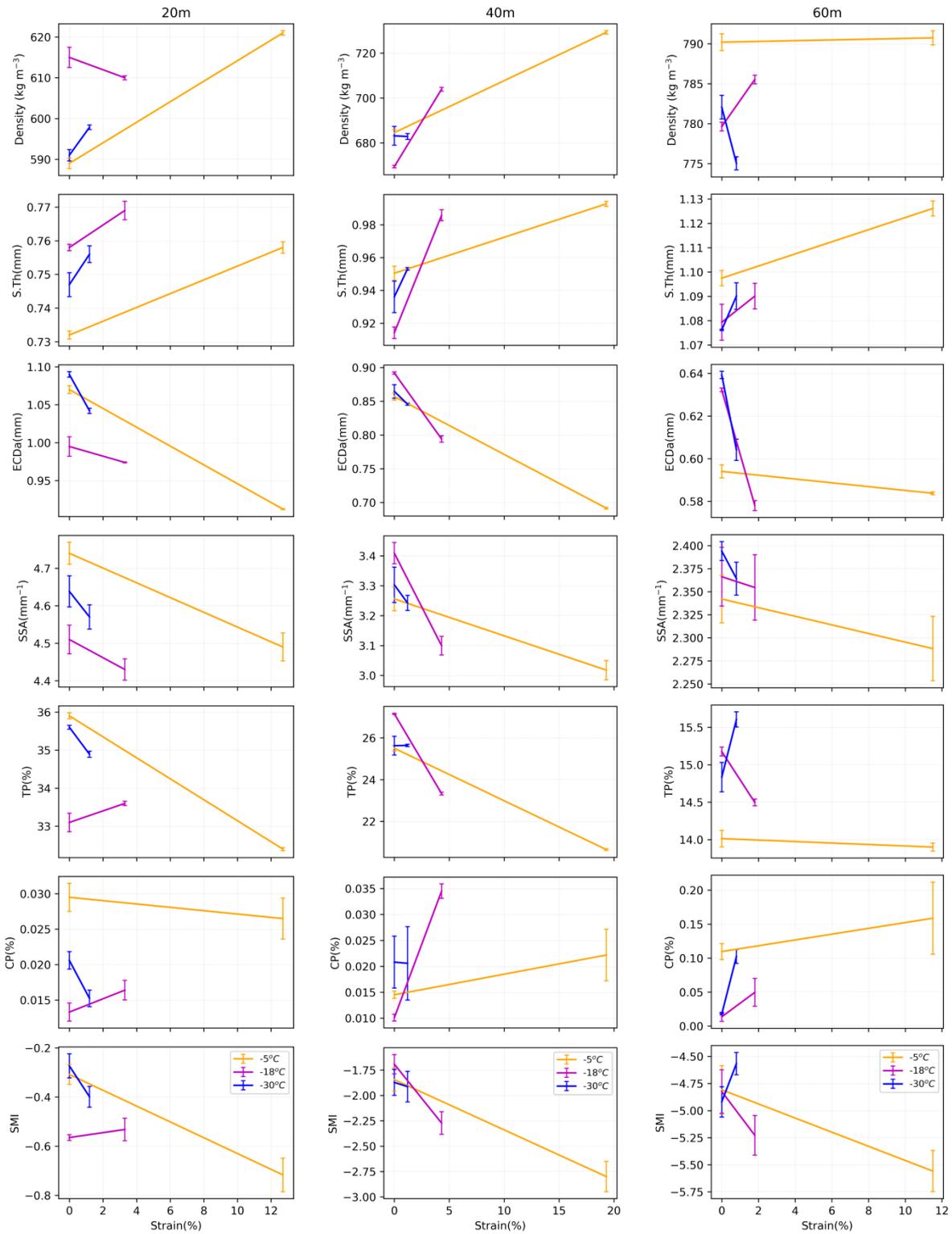
Figure 3: Density, structure thickness (S.Th), area-equivalent circle diameter (ECDa), specific surface area (SSA), total porosity (TP), closed porosity (CP), and structure model index (SMI) of the firn samples before and after creep at three temperatures (orange, magenta, and blue lines)

296 from depths of 20 m, 40 m and 60 m. Error bars indicate the variation of each microstructural

297 parameter as derived from three different VOIs of the same sample.

298

299

300 m, and 60 m samples, respectively. The 44 kg m^{-3} unexpectedly outnumbers the 32 kg m^{-3},

301 implying that the densification of firn is also affected by other undetermined factors, e.g. the

302 effect of inclusions, in addition to the stress and temperature.

303

304 Another way to investigate microstructure changes before and after creep tests is to compare their

305 grain sizes using thin sections. As an example, **Figure 4** shows optical micrographs of thin

306 sections made from the –5°C sample at 40 m before and after creep to a strain of 19.3%, where

307 the significant reduction in grain size from 0.8 ± 0.67 mm to 0.5 ± 0.32 mm implies the

308 occurrence of recrystallization during testing. However, it is also unclear at what strain

309 recrystallization

310

311

312

313

314

315

316

317

318
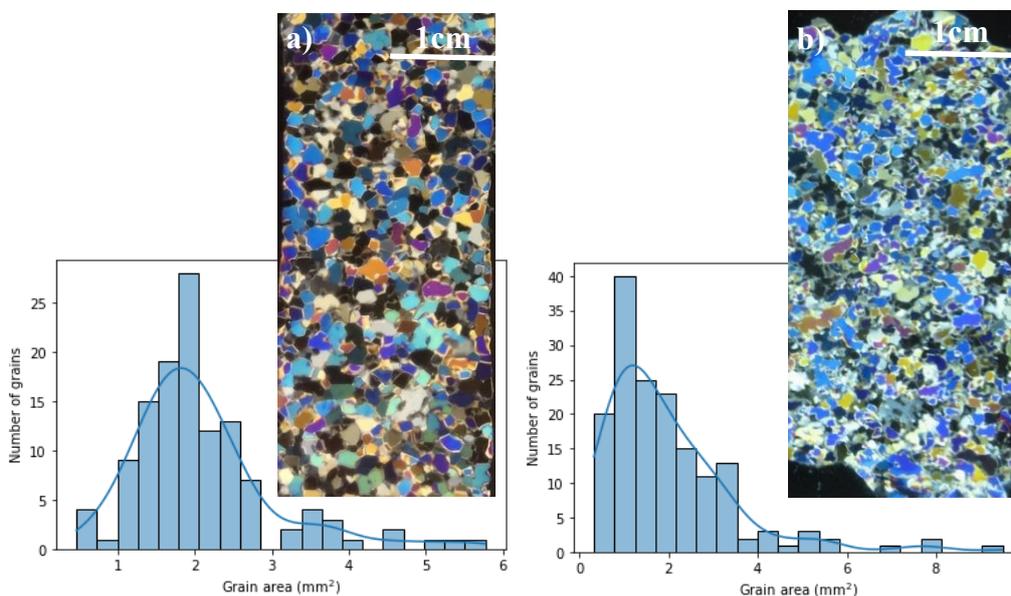
Figure 4: Optical micrographs of thin sections, and the distribution of grain sizes for the 40 m sample at –5°C (a) before and (b) after creep (19.3% strain).

was initiated in each test, as noted in Li and Baker (2022a). Recrystallization occurs frequently at a temperature higher than the homologous temperatures of 0.9 T_m. However, no evidence was found for recrystallization after testing at the relatively cold –18°C and –30°C conditions, probably due to the small creep strains at these relatively low temperatures. The creep mechanisms for these samples, and whether the mechanisms were different at different temperatures, could not be determined from the micro-CT-derived microstructural observations alone, because the micro-CT can only capture the microstructure before and after creep. Instead, plots of both strain vs. time and strain rate vs. strain can be used to elucidate the onset of recrystallization during creep (Sections 3.3 and 3.4; Ogunmolasuyi, et al., 2023).

3.3 *Relationship between strain and time*

Figure 5 shows the strain vs. time creep curves. The specimens at –5°C at 20 m and –18°C at 20 m, 40 m, and 60 m, show decelerating transient creep and quasi-viscous steady-state creep, while the specimens at –5°C at 40 m and 60 m show transient, secondary, and accelerating tertiary creep. Note that the curves from the –30°C specimens are not easily interpreted due to a large amount of noise arising from both the insufficient resolution of a linear voltage differential transducer (Li and Baker, 2022a) and the very small strains. The transient creep stage may be caused by strain hardening that occurs from the yield point to the ultimate strength (Glen, 1955; Jacka, 1984). The

341   plastic deformation is accommodated by an increase in dislocation density through dislocation

342   multiplication or the formation of new dislocations (Frost and Ashby, 1982; Duval et al., 1983;

343   Ashby and Duval, 1985), which leads to an increase of the firn strength as the dislocations

344   become pinned or tangled, and thus more difficult to move. The initial decrease of creep rate may

345   also be related to the rearrangement of dislocations into a more stable pattern through a dragging

346   mechanism (Weertman, 1983) for the –5°C specimens. The tertiary creep stage may be associated

347   with strain softening deriving either from the thermally-activated processes at the high

348   homologous temperature approaching the melting point of ice, or from recrystallization (Li and

349   Baker, 2022a). Clearly, the creep rate of firn is sensitive to temperature under constant stress at a

350   given depth, *viz.*, the creep rate increases with increasing temperature (**Figure 5**). Incidentally,

351   there is no evidence of the onset of recrystallization in the creep curves themselves despite the

352   thin-section observation that –5°C specimens clearly underwent recrystallization during creep

353   (Section 3.2).

354

355   A modified Andrade-like equation $\varepsilon = \beta t^{k} + \varepsilon_0$ in Li and Baker (2022a) was used to describe the

356   transient creep behavior of the firn, in which the primary creep was well represented in black

357   dashed lines on the creep curves in **Figure 5**. The time exponent k, derived from the above

358   equation, ranges from 0.34–0.69: the data for the –30°C specimens are excluded since the noise in

359   the results makes them uninterpretable. These k values are also smaller than those from

360   monocrystalline and bicrystalline ice: 1.9 ± 0.5, 1.5 ± 0.2, and 1.3 ± 0.4 (Li and Baker, 2022a and

361   references therein). We also note that the k values from the specimens at –5°C from 20–60 m

362

363

364

365
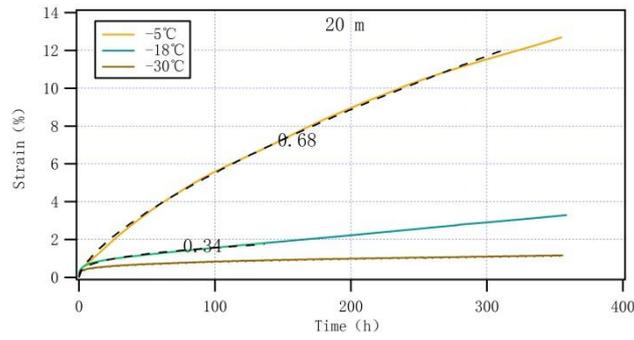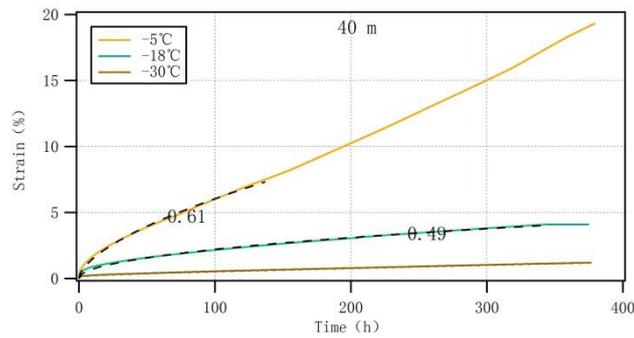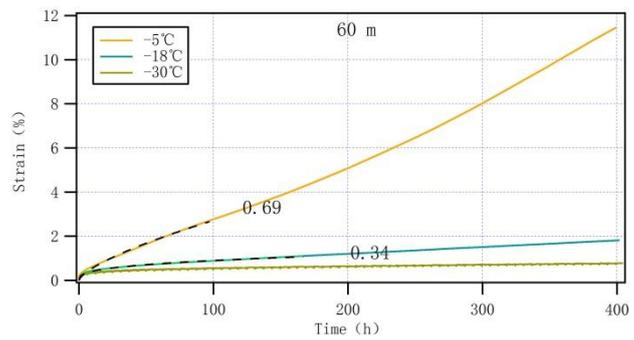
Figure 5: Strain vs. time for firn specimens at –5°C (yellow lines), –18°C (blue lines), and –30°C (brown lines), from depths of 20 m (applied stress 0.21 MPa), 40 m (0.32MPa) and 60 m (0.43MPa). The black dashed curves represent fits to a modified Andrade-like equation with the time exponents indicated on the curves, if any.

370

371

(0.68, 0.61, and 0.69), and at –18°C from 40 m (0.49) are greater than 0.33, while the k value from the –18°C specimens at 20 m (0.34) and 60 m (0.34) are close to 0.33 that is usually

obtained for full-density polycrystal ice. Interestingly, an evident relationship between the density of firn and the k values, regardless of the effect of stress (Li and Baker, 2022a) and temperature, remains unknown. A greater k value signifies faster deformation. The k values derived for firn are generally higher than those for polycrystalline ice, implying that the higher firn deformation rates compared to those of ice are likely related to the fewer grain-boundary constraints with more void space in firn (Li and Baker, 2022a; Li, 2023b). Clearly, the above k values, which increased with increasing temperature (**Figure 5**), indicate that deformation is easier because of the lower viscosity at the higher temperature. Thus, k seems to be a state variable with respect to temperature. In addition, k values greater than 0.33 may be related to the decrease of viscosity of the firn specimens (Freitag et al., 2002; Fujita et al., 2014). k values lower than 0.33 observed under constant load and temperature occurred at relatively low effective stresses (Li and Baker, 2022a). However, the steady decrease of k values from -5°C to -18°C remains further investigation. Alternatively, the enhanced cohesion strength in the firn, which resulted from both the ice matrix with higher purity and the stronger bond connection of inter-grains, increases the viscosity of test samples and lowers the k value to less than 0.33.

3.4 *Relationship of strain rate to strain*

Figure 6 shows log strain rate vs. strain plots from all the -5°C and -18°C specimens; the -30°C samples are excluded due to noise. The evolution of the strain rate is characterized more clearly in **Figure 6** than in **Figure 5**. Clearly, the strain rate is also a state variable of temperature, where the strain rate increases with increasing temperature for a given strain at a given depth (**Figure 6**; **Table 2**). The strain rate minimum at the secondary creep stage (SRmin) and the strain at the

Table 2. Observed and inferred strain rate minima and strains observed at the strain rate minima.

20 m	SRmin s^{-1}	PC1-SRmin s^{-1}	PC2-SRmin s^{-1}	PC3-SRmin s^{-1}	Strain %
–5°C	5.53×10^{-6}	***5.53×10^{-6}***	*1.68×10^{-6}*	*2.56×10^{-7}*	11.8
–18°C	1.36×10^{-6}	***1.36×10^{-6}***	*2.29×10^{-7}*	*2.45×10^{-8}*	1.81–2.9
–30°C(U)	–	7.14×10^{-7}	2.17×10^{-7}	3.3×10^{-8}	–
–30°C(L)	–	3.16×10^{-8}	9.6×10^{-9}	1.46×10^{-9}	–

40 m	SRmin s^{-1}	PC1-SRmin s^{-1}	PC2-SRmin s^{-1}	PC3-SRmin s^{-1}	Strain %
–5°C	1.03×10^{-5}	*3.39×10^{-5}*	***1.03×10^{-5}***	*1.57×10^{-6}*	7.5
–18°C	1.4×10^{-6}	*8.32×10^{-6}*	***1.40×10^{-6}***	*1.5×10^{-7}*	4.1
–30°C(U)	–	4.37×10^{-6}	1.33×10^{-6}	2.03×10^{-7}	–
–30°C(L)	–	1.94×10^{-7}	5.88×10^{-8}	8.97×10^{-9}	–

60 m	SRmin s^{-1}	PC1-SRmin s^{-1}	PC2-SRmin s^{-1}	PC3-SRmin s^{-1}	Strain %
–5°C	5.59×10^{-6}	*1.21×10^{-4}*	*3.67×10^{-5}*	***5.59×10^{-6}***	2.7
–18°C	5.33×10^{-7}	*2.96×10^{-5}*	*4.99×10^{-6}*	***5.33×10^{-7}***	1.1–1.8
–30°C(U)	–	1.56×10^{-5}	4.74×10^{-6}	7.21×10^{-7}	–
–30°C(L)	–	6.91×10^{-7}	2.1×10^{-7}	3.19×10^{-8}	–

The SRmin without the prefix is the observed values during creep, while the SRmin with a prefix is the inferred values. Note that PC-SRmin is the abbreviation of the post-calibration SRmin, and that –30°C(U) and –30°C(L) indicate the upper and lower bound from the –30°C samples from 44.8 kJ mol⁻¹ and 113 kJ mol⁻¹, respectively. PC1-SRmin, PC2-SRmin, and PC3-SRmin are described in **Appendix B**. The symbol – indicates the unavailable values of SRmin and the strain value at the SRmin observed during creep. For the italics highlighted, see **Appendix B**.

409

410

411
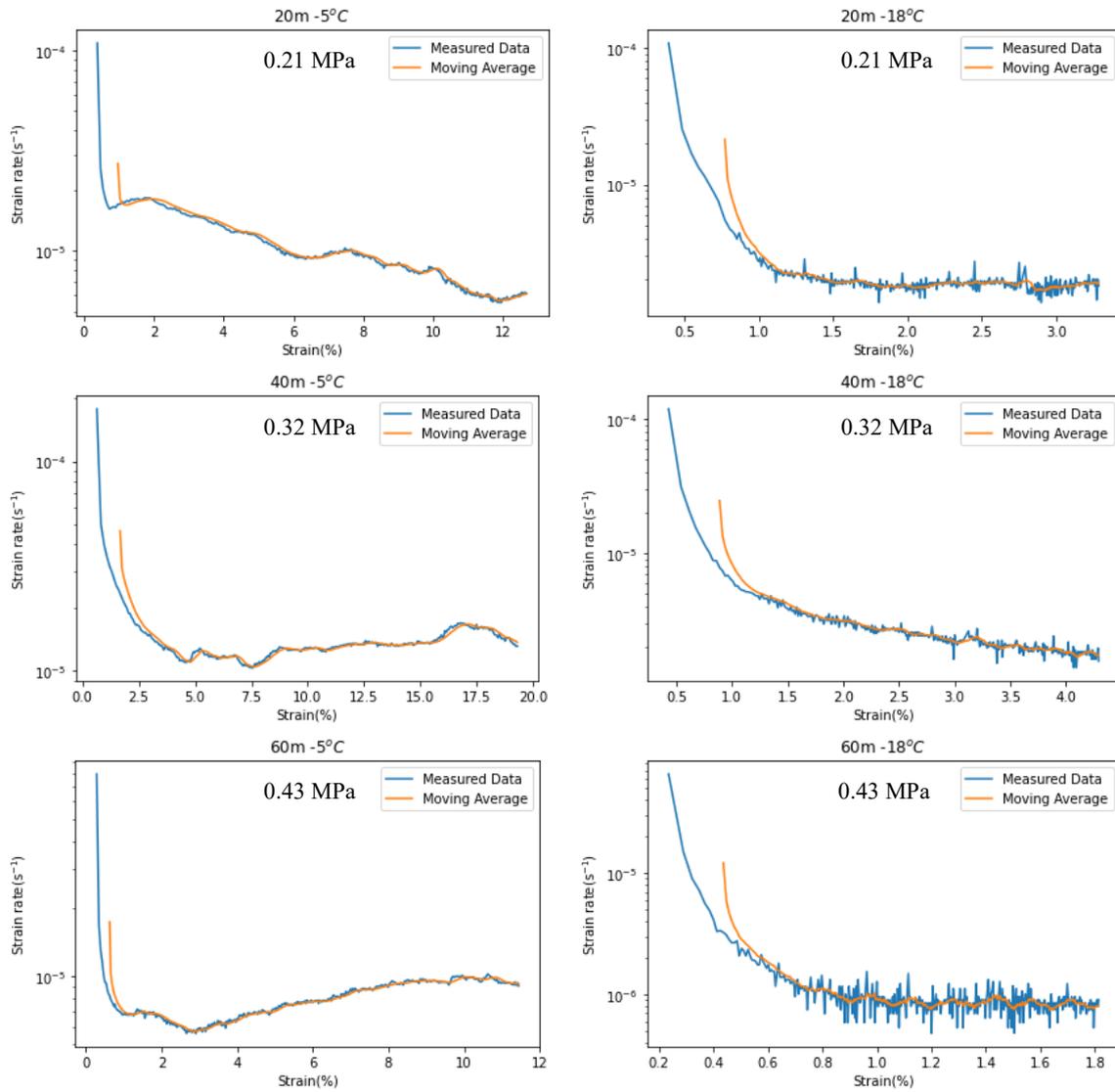
Figure 6: Log strain rate vs. strain from the firn specimens at temperatures of -5°C and -18°C

from depths of 20 m (applied stress 0.21 MPa), 40 m (0.32MPa) and 60 m (0.43MPa). Samples

from -30°C are not shown due to the very large noise. The blue lines represent discrete strain rates,

which are calculated by extracting the strain data hourly, while the orange lines represent a

moving average of 15 moving windows with respect to the strain.

SRmin for all the –5°C and –18°C specimens are shown in **Figure 6** and **Table 2**. The SRmin was

reached at a strain of 11.8%, 7.5% and 2.7% for the –5°C specimens from depths of 20 m, 40 m,

25

421   and 60 m, respectively, consistent with strains at the SRmin decreasing with increasing depth at a

422   given temperature in **Figure 8** and **Table 4** in Li and Baker (2022a). For the –18 °C specimens,

423   the SRmin occurred over a range of strains from 1.81–2.9% at 20 m, at a fixed strain of 4.1% at

424   40 m, and at a strain oscillating between 1.1 and 1.8% at 60 m. These values of strain at different

425   SRmin values are different from those usually observed at strains of 0.5–3% for fully-dense ice

426   (Cuffey and Paterson, 2010, and references therein), implying different mechanical behavior

427   between firn and pure ice (Duval, 1981; Mellor and Cole, 1983; Jacka, 1984; Li et al., 1996;

428   Jacka and Li, 2000; Song et al., 2005, 2008; Cuffey and Paterson, 2010). Overall, the strain at the

429   SRmin is greater with lower density and higher temperature, e.g. 11.8% strain from the –5°C

430   specimens at 20 m, and 4.1% strain from the –18°C specimens at 40 m. This is likely due to the

431   effect of strain hardening on density and temperature (Li, 2023b). Additionally, tertiary creep is

432   observed during both quasi-steady state deformation, particularly in the –5°C specimens at depths

433   of 40 m and 60 m, and in the ascending stage, as seen in the –5°C and –18°C specimens at 20 m,

434   along with the –18°C specimen at 40 m. This mechanical behavior is facilitated by lower firn

435   density, increased effective stress, and elevated creep temperatures. For instance, in the –5°C

436   specimens at 20 m, strain softening primarily results from recrystallization (Duval, 1981; Jacka,

437   1984; Jacka and Li, 2000; Song et al., 2005; Faria et al., 2014). Also, the activation of easy slip

438   systems contributes to this process (Jonas and Muller, 1969; Duval and Montagnat, 2002; Alley et

439   al., 2005; Horhold et al., 2012; Fujita et al., 2014; Eichler et al., 2017). It is noteworthy that Jacka

440   and Li (1994) observed that steady-state tertiary ice creep, which is marked by stable grain size, is

441   influenced more by applied stresses than by temperature. This finding suggests that there exists a

442   balance between the activation energies required for grain growth and subdivision at a specific

443   temperature.

444

445   3.5 *Apparent activation energy for creep*

446   Experimental observations of the SRmin are limited, as they only occurred for the –5°C and at –

447   18°C specimens at each depth (**Table 2**). It is hard to achieve the SRmin for all firn specimens in

448   laboratory environments (Landauer, 1958), especially under low temperatures and stresses such as

449   those from the –30°C specimens in this work. To this end, we offer the various possibilities of the

450   SRmin using the evidence we have. The value of the apparent activation energy of creep, Q_c (kJ

451   mol^{-1}), is equal to the slope of a line fitted $\ln \dot{\varepsilon}$ versus $1/T$ as did in Goldsby & Kohlstedt (1997;

452   2001), using the Arrhenius relation $\dot{\varepsilon} = B\sigma^n \exp(-\frac{Q_c}{RT})$, where $\dot{\varepsilon}$ (s^{-1}) is the strain rate, B (s^{-1}

453   Pa^{-n}) is the material parameter, σ (MPa) is the applied stress, n is the creep (stress) exponent, R

454   (8.314 J mol^{-1} K^{-1}) is the gas constant, and T (K) is Kelvin temperature. First, the estimation of

455   Q_c is based on *only* two SRmin values from the –5°C and –18°C samples at each depth (**Table 2**).

456   Glen-King's model $\dot{\varepsilon} = A\exp(-Q_c/RT) = B\sigma^n \exp(-Q_c/RT)$ treats the pre-factor A, material

457   parameter B, and stress exponent n as constants (Glen, 1955; Goldsby and Kohlstedt, 2001). This

458   simplification is valid by using the unifying concept of normalized effective stress. The effective

459   stress captures the complex multi-physical behavior of the two-phase ice-air system, accounting

460   for: 1) The incompressibility of individual ice grains versus the compressibility of the porous ice

461   skeleton, 2) The coupled flow of ice and air; and 3) The interplay between different strain

462   components (axial, radial, volumetric, and true). This framework is grounded in the principles of

463   poromechanics, originally developed for soils and later applied to snow and ice (Gubler, 1978;

464   Hansen and Brown, 1988; Mahajan and Brown, 1993; Chen and Chen, 1997; Lade and deBoer,

1997; Ehlers, 2002; Khalili et al., 2004; Gray and Schrefler, 2007; daSilva et al., 2008; Nuth and

Laloui, 2008). The variability in density for the samples from 20-m depth on the mechanical

behavior are negligible due to a small difference (up to ~4%), between samples, which falls

within an acceptable error range in previous studies. This is likely related to multiple factors,

including the intrinsic properties of the samples, e.g. inclusions (impurities, dust, bubbles,

clathrate hydrates), the effects of deformation and partial annealing of firn due to stress

distribution and temperature changes during drilling, extraction, transportation, or storage, and the

fact that the samples are taken from adjacent parts of the core, and might capture heterogeneous

density layers, as well as potential measurement errors associated with the equipment used. The

Q_c values from the 20 m, 40 m, and 60 m specimens were calculated to be 61.4 kJ mol^{-1}, 87.3 kJ

mol^{-1}, and 102.8 kJ mol^{-1}, respectively (**Figure 7**). Based on the three SRmin from the –5°C and –

18°C samples at 60 m in this work, and from –10°C samples at 60 m in Li and Baker (2022a), a

Q_c value for the 60 m specimen was calculated to be 100.7 kJ mol^{-1}. To see whether or not these

above Q_c values are reliable, we estimated the activation energy of grain-boundary

diffusion/viscosity, Q_{gbd} (kJ mol^{-1}), using the relation $K = \left(D_t^2 - D_0^2\right)/t = k\exp(-Q_{gbd}/RT)$,

in an alternative form of $Q_{gbd} = -R\left[\partial \ln K/\partial\left(1/T\right)\right]$, where K is the observed rate of grain

growth (mm^2 a^{-1}), D_0^2 and D_t^2 are the measured mean grain area (mm^2) in a firn sample at the

onset of the creep ($t = 0$), and at the end time of the creep (t-year), and k is a constant grain

growth factor. The grain growth rates are plotted on a logarithmic scale against the reciprocal of T

(**Figure 7**). For changes in grain size from the related specimens before and after creep see **Table

3**. Correspondingly, the Q_{gbd} values calculated were 41.4 kJ mol^{-1}, 40.8 kJ mol^{-1}, and 40.9 kJ

mol^{-1} for the specimens at 20 m, 40 m, and 60 m, respectively. These Q_{gbd} values are comparable

to the values of 40.6 kJ mol^{-1} obtained in laboratory experiments on polycrystalline ice (Jumawan, 1972), and 42.4 kJ mol^{-1} from 13 polar firn cores (Cuffey and Paterson, 2010) for grain-boundary self-diffusion of polycrystalline ice. Further, the ratio of Q_{gbd}/Q_c is 0.67, 0.47, and 0.4 for the 20 m, 40 m, and 60 m specimens, respectively. We noted that the ratio of 0.67 for Q_{gbd}/Q_c was recommended by Hobbs (1974) and Cuffey and Paterson (2010). The Q_c values calculated using the Arrhenius relation for the 40 m and 60 m specimens are likely greater than the actual values, and hence are seemingly less reliable. There is little difference between the two-SRmin-derived Q_c value (102.8 kJ mol^{-1}) and the three-SRmin-derived Q_c value (100.7 kJ mol^{-1}), implying that these two avenues for calculating Q_c have equal utility. Moreover, the above Q_{gbd} values are lower than the 48.6 kJ mol^{-1} that was inferred by the grain growth rate for firn samples with densities ranging from 320–650 kg m^{-3} from cores drilled at the South Pole, Antarctic (Gow, 1969), which makes a ratio of 0.67 for Q_{gbd}/Q_c an unreliable sole-criterion. In short, it is difficult to assess the reliability of both Q_c and Q_{gbd}, as discussed above due to their scatter and debates in the current literature. Thus, these Q_c values estimated in this work, ranging from 61.4–102.8 kJ mol^{-1}, are reasonable, aligning with the literature range of 44.8–113 kJ mol^{-1} (**Table 4**).

Table 3. Grain area (mm^2) measured from optical thin sections for samples at –5ºC, –18ºC, and –30ºC from depths of 20 m, 40 m, and 60 m before and after creep.

| Depth	20 m		40 m		60 m	
T/ºC	Before	After	Before	After	Before	After
–5	0.29±0.25	0.42±0.28	0.53±0.32	0.79±0.67	0.78±0.67	0.97±0.8
–18	0.29±0.25	0.34±0.2	0.53±0.32	0.7±0.42	0.78±0.67	0.9±0.59
–30	0.29±0.25	0.31±0.17	0.53±0.32	0.57±0.34	0.78±0.67	0.81±0.56

507

508 A great challenge is the estimation of the Q_c using the SRmin including the –30ºC specimens,

509 whose SRmin shows high variability due to the extraordinarily slow strain rate at low

510 temperatures. This difficulty cannot be resolved by extrapolating experimental data (Sinha, 1978;

511 Hooke et al., 1980), e.g. the use of Andrade's law (Glen, 1955). Instead, we turned our focus to

512 studying the relationship between the SRmin and temperature by constraining our data in a wide

513 range of Q_c values reported in existing literature presented in **Table 4**. Clearly, there is a larger

514 scatter of Q_c values for firn than for ice. The increase of Q_c from mono-crystalline and

515 bi-crystalline to polycrystalline ice implies that the greater the reduction in the constraint from

516 grain boundaries, the greater is Q_c. Alternatively, firn creep is easier than that of polycrystalline

517 ice due to either the easier sliding of grains in firn along more directions in the more porous and

518 heterogeneous structure (Section 3.3), or the decrease of viscosity associated with inclusions (e.g.

521

522

523
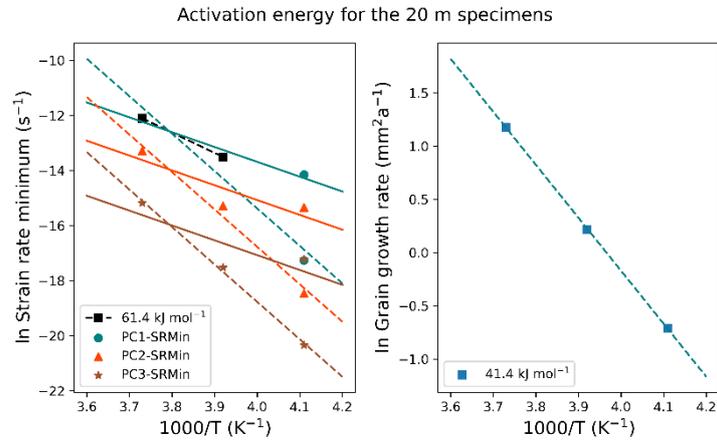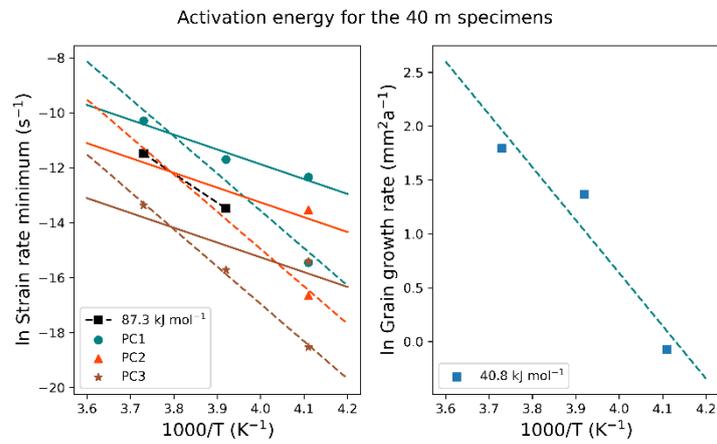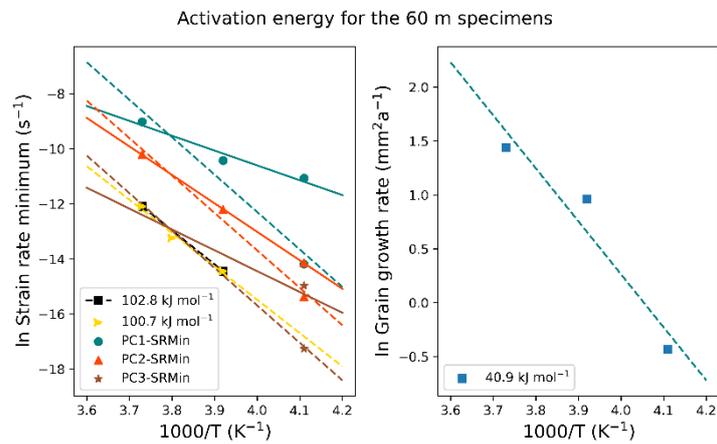
Figure 7: Arrhenius plots to estimate the apparent activation energy of creep (Q_c; left panel) and

the apparent activation energy of grain-boundary diffusion (Q_{gbd}; right panel) from the firn

specimens noted. The teal, orange, and brown solid lines are the upper bound (44.8 kJ mol^{-1}) of

PC1-SRmin, PC2-SRmin, and PC3-SRmin, respectively, while the teal, orange, and brown dashed

528 lines are the lower bound (113 kJ mol^{-1}) of PC1-SRmin, PC2-SRmin, and PC3-SRmin,

529 respectively (Table 2). The teal circles, the orange triangles, and the brown stars are the data in

530 Table 2. The black dashed lines are from *only* two SRmins at –5ºC and –18ºC (the black squares

531 are the data measured), whose Q_c is indicated in each subfigure. The yellow dashed line is from

532 the three SRmins at –5ºC, –18ºC in this work, and –10 ºC from Li and Baker (2022a) (the yellow

533 triangles are the measured data), whose Q_c is 110.7 kJ mol^{-1}. The blue dashed lines (right panel)

534 are from grain growth rate at three temperatures (the blue squares are the observed data), whose

535 Q_{gbd} is indicated in each subfigure.

536

537

538 Table 4. Apparent activation energy for the creep of firn and ice, Q_c, reported in literature.

Q_c kJ mol^{-1}	Sample	Density kg m^{-3}	Temperature ºC	Methods	Source
58.6–113	Firn	~400	[–13.6, –3.6]	Uniaxial/Hydrostatic Compression	Landauer (1958)
44.8–74.5	Firn/Bubbly Ice	440–830	[–34.5, –0.5]	Uniaxial Unconfined Compression	Mellor and Smith (1966)
54	Firn/Bubbly Ice	Undetailed	[−28, −16]	Shear Deformation of Boreholes	Paterson (1977)
~72.9	Firn	320–650	Unnecessary	Grain Growth Rate	Gow (1969)
69 ± 5	Firn	423 ± 8	[–19, –11]	Triaxial Compression	Scapozza and Bartelt (2003)
~60	Artificial/Natural Ice (South Pole)	~917	–15	Torsion Creep Test	Pimienta and Duval (1987)
61	Polycrystalline Ice	~917	–9.6	Hydrostatic Pressure	Duval et al. (1983)
78	Monocrystalline Ice	~917	[–30, –4]	Derived from Bicrystal Ice	Homer and Glen (1978)
75	Ice Bicrystal	~917	[–30, –4]	Tensile Test Parallel to Grain-boundary	Homer and Glen (1978)

539

540

Baker and Gerberich, 1979; Goodman et al., 1981) that facilitate the intra- and inter-grain sliding

(Salamatin et al., 2009). In principle, Q_c of firn should exceed that for polycrystalline ice.

Intriguingly, some reported Q_c values from firn are less than that for ice, meaning the degree of

spatial freedom in the ice-matrix is limited by the topological structure of the firn (Liu et al.,

2022). Incidentally, the effective stress of porous materials is determined by not only its porosity,

but also other factors, e.g. the microstructural topology (Liu et al., 2022) and the impurity types

and concentrations in the firn. However, this issue is beyond the scope of this work. In seeking a

conclusion, we evaluated the dependence of creep activation energy on firn density. The data

indicate no discernible relationship between these two parameters (**Fig. 8**). In summary, a Q_c for

firn, which ranges from 44.8–113 kJ mol^{-1}, is plausible due to the intrinsic nature of natural firn

that has a far more complicated and changeable microstructure than ice.

552
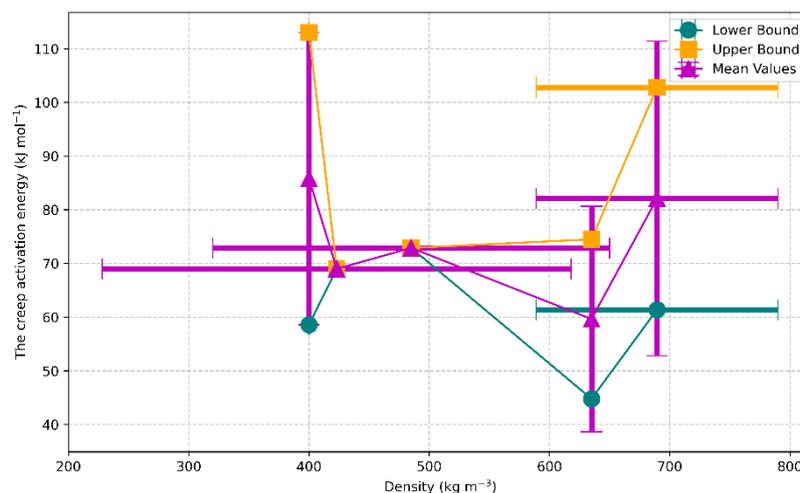
Figure 8: Plots of the creep activation energy vs. firn densities. For each density, three values are

shown: the lower bound (minimum activation energy, teal), the upper bound (maximum activation

energy, orange), and the mean value (magenta). Error bars represent the standard deviation of the

557   mean. Data are sourced from Table 4 and the present study.

558

559

560   The value of the stress exponent n is determined by plotting the line fit the logarithm relation of

561   the steady-state strain rate, $\dot{\varepsilon}$, versus the effective stress, σ, and is, thus, the slope of this line

562   from the measured SRmins (**Table 2**). We determined stress exponent (n) values of approximately

563   0.1 and –1.2 for the –5°C and –18°C samples based on observed data, respectively. This result

564   directly contradicts the value of $n \approx 4.3$ reported from the same Greenland firn core by Li and

565   Baker (2022a). Further, these values fall entirely outside the established range of ~1 to ~7.5

566   (mean ~4.25 ± 3.25) documented across decades of ice mechanics literature (Glen, 1955; Hansen

567   and Landauer, 1958; Butkovich and Landauer 1960; Kamb, 1961; Paterson and Savage, 1963;

568   Higashi et al, 1965; Mellor and Testa, 1969; Raymond, 1973; Hooke, 1981; Thomas et al., 1980;

569   Duval et al., 1983; Weertman, 1983,1985; Azuma and Higashi, 1984; Pimienta and Duval, 1987;

570   Budd and Jacka, 1989; Jacka and Li, 1994; Goldsby and Kohlstedt, 2001; Bindschadler et al.,

571   2003; Cuffey, 2006; Chandler et al. 2008; Cuffey and Kavanaugh, 2011; McCarthy et al., 2017;

572   Millstein et al., 2022; Colgan et al., 2023; Li, 2025). The wide range of reported n-values is

573   governed by a complex interplay of deformation mechanisms—including grain boundary sliding,

574   diffusion (lattice and grain boundary), and dislocation processes, e.g. hard-slip-dominated,

575   dislocation-accommodated grain boundary sliding, and grain boundary sliding-limited basal

576   dislocation—across varying stresses, temperatures, crystalographic fabrics, impurity contents, and

577   grain-size-to-sample-size ratios. We attribute the significant discrepancy in these findings to the

578   experimental conditions. The lower temperatures used (down to –30°C) induce slower strain rates,

579 which prevented the tests from reaching a critical strain rate minimum (SRMin). Therefore, to

580 accurately estimate the activation energy for deformation, it is necessary first to calibrate the

581 SRMin value for all noised samples. A constant stress exponent value of $n \approx 4.3$ (Li and Baker,

582 2022a) was used to compute the activation energy. This necessary simplification—an

583 acknowledgement of current methodological limitations rather than a dismissal of the underlying

584 physics—introduces a key uncertainty that highlights the need for future advancements in

585 observational methodology within firn research. To proceed, the post-calibration SRmins for the –

586 5°C and –18°C samples are highlighted in **Table 2** (see **Appendix B** in detail). It is important to

587 note that the stress exponent does not depend on the density of the tested samples, thereby

588 negating any basis for discussing a relationship between the stress exponent and sample density.

589 Instead, variations in stress corresponding to density variations are manifested in the strain rate,

590 ensuring that the derivation of the stress exponent and activation energy remains consistent. From

591 here on we only discuss the applied stress since there is little difference between the effective

592 stress and applied stress for calculating the stress exponent (Li and Baker, 2022a). Based on both

593 the reported range of Q_c and the two observed SRmins at −5°C and −18°C, the SRmins for the

594 −30°C samples are inferred (**Table 2**), using the Arrhenius relation. Also, based on both the

595 observed and inferred SRmins with the upper and lower bounds (**Table 2**), a series of fitted

596 functions are then found between the SRmin and the reciprocal of the temperature (°C), $1/T_c$:

597

598   20-m samples:

599

$$\begin{cases} \text{SRMin} = -3 \times 10^{-5}/T_c - 7 \times 10^{-7} [R^2 = 0.988; \text{PC}1(\text{L}\,20)] \\ \text{SRMin} = -3 \times 10^{-5}/T_c - 2 \times 10^{-7} [R^2 = 1; \text{PC}1(\text{U}\,20)] \\ \text{SRMin} = -1 \times 10^{-5}/T_c - 3 \times 10^{-7} [R^2 = 1; \text{PC}2(\text{L}\,20)] \\ \text{SRMin} = -9 \times 10^{-6}/T_c - 2 \times 10^{-7} [R^2 = 0.987; \text{PC}2(\text{U}\,20)] \\ \text{SRMin} = -2 \times 10^{-6}/T_c - 6 \times 10^{-8} [R^2 = 0.998; \text{PC}3(\text{L}\,20)] \\ \text{SRMin} = -1 \times 10^{-6}/T_c - 3 \times 10^{-8} [R^2 = 0.976; \text{PC}3(\text{U}\,20)] \end{cases},$$

600   40-m samples:

601

$$\begin{cases} \text{SRMin} = -2 \times 10^{-4}/T_c - 4 \times 10^{-6} [R^2 = 0.988; \text{PC}1(\text{L}\,40)] \\ \text{SRMin} = -2 \times 10^{-4}/T_c - 2 \times 10^{-6} [R^2 = 1; \text{PC}1(\text{U}\,40)] \\ \text{SRMin} = -6 \times 10^{-5}/T_c - 2 \times 10^{-6} [R^2 = 1; \text{PC}2(\text{L}\,40)] \\ \text{SRMin} = -6 \times 10^{-5}/T_c - 1 \times 10^{-6} [R^2 = 0.987; \text{PC}2(\text{U}\,40)] \\ \text{SRMin} = -1 \times 10^{-5}/T_c - 3 \times 10^{-7} [R^2 = 0.998; \text{PC}3(\text{L}\,40)] \\ \text{SRMin} = -9 \times 10^{-6}/T_c - 2 \times 10^{-7} [R^2 = 0.976; \text{PC}3(\text{U}\,40)] \end{cases},$$

602   60-m samples:

603

$$\begin{cases} \text{SRMin} = -7 \times 10^{-4}/T_c - 2 \times 10^{-5} [R^2 = 0.988; \text{PC}1(\text{L}\,60)] \\ \text{SRMin} = -6 \times 10^{-4}/T_c - 6 \times 10^{-6} [R^2 = 1; \text{PC}1(\text{U}\,60)] \\ \text{SRMin} = -2 \times 10^{-4}/T_c - 7 \times 10^{-6} [R^2 = 1; \text{PC}2(\text{L}\,60)] \\ \text{SRMin} = -2 \times 10^{-4}/T_c - 4 \times 10^{-6} [R^2 = 0.987; \text{PC}2(\text{U}\,60)] \\ \text{SRMin} = -3 \times 10^{-5}/T_c - 1 \times 10^{-6} [R^2 = 0.998; \text{PC}3(\text{L}\,60)] \\ \text{SRMin} = -3 \times 10^{-5}/T_c - 7 \times 10^{-7} [R^2 = 0.976; \text{PC}3(\text{U}\,60)] \end{cases},$$

604

605   where PC1(L20) and PC1(U20) indicate the lower and upper bound values of the post-calibration

606   SRmins from the 20 m samples (**Table 1**), and other symbols are similarly formatted, e.g.

607   PC1(L40), PC1(U40), PC1(L60), PC1(U60), and so on. These relationships are plotted in **Figure**

608   **8**, where the SRmin vs. $1/T_c$ plots from the three depths are almost the same shape, implying that

609   the SRmin is dependent on the temperature at a constant stress. It is important to note that the

610   average (minimum) strain rate for the secondary creep stage for a given temperature increases

611   with increasing depth/density of the samples (**Figure 8**; **Table 2**). This is opposite to a decrease of

612   the SRmin at a fixed stress and temperature in **Figure 8** and **Table 4** in Li and Baker (2022a).

613   These changes in SRmin are irrespective of the stress (**Appendix A**). The temperature plays a

614   predominant role during firn creep for a given density of sample at a constant stress. An

615   interesting question on firn creep at a specific temperature is whether the SRmin slows down or

616   speeds up with decreasing density of firn. Certainly, natural firn samples raise the complexity in

617   interpreting the firn creep due to the influences both from inclusions (Li and Baker, 2022a and

618   references therein; Li, 2024), and from the topology of the microstructures (Liu et al., 2022). In

619   addition, there is a broad spread of the SRmin at each depth, in which the SRmin varies by several

620   times, even one order of magnitude or more between the different possibilities of post-calibration

621   SRmins (**Figure 8**), implying that the microstructure of the sample significantly influences the
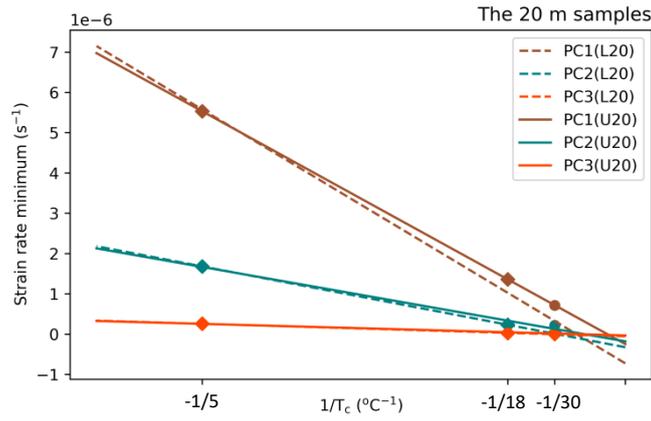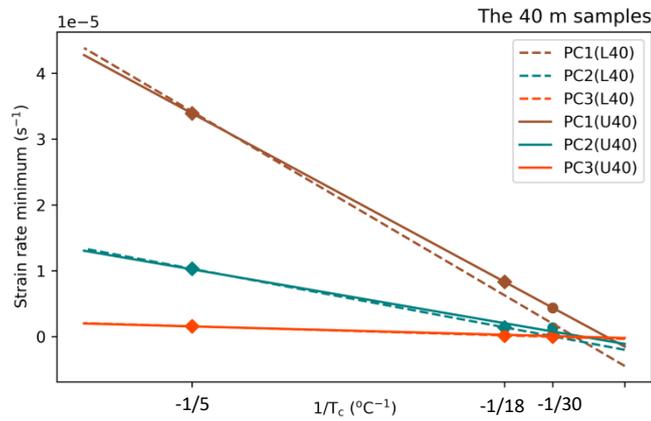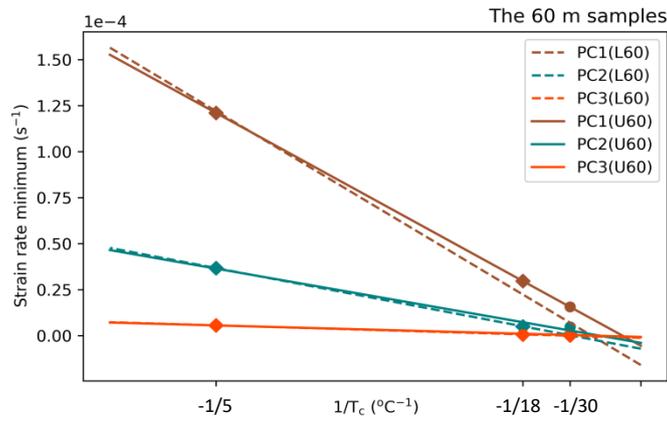
Figure 9: Plots of the strain rate minimum versus the reciprocal of temperature. PC1(L20) and PC1(U20) indicates the lower and upper bound, respectively, from the 20 m samples via PC1 as noted in Table 2, and so on. The circles indicate the upper bound data measured and inferred, while the squares indicate the lower bound data. The dashed line is the fit from the lower bound, while the solid line is the fit from the upper bound.

644

645 process of the creep of firn. Moreover, it is hard to generalize a universal formula for predicting

646 the SRmin at temperatures below −30°C, where the SRmins becomes negative (**Figure 8**). Thus,

647 there is a need for an in-depth understanding of the polar firn creep behavior in secondary creep

648 stage.

649

650 To illustrate the differences between the Q_c values calculated from PC1-SRmin, PC2-SRmin,

651 and PC3-SRmin, we have plotted them in **Figure 7**. Interestingly, the Arrhenius plots of the

652 natural logarithm of strain rate with $1000/T$ (**Figure 7**) are similar to those observed by Glen

653 (1955) and Homer and Glen (1978), implying that there is no significant difference in the creep

654 mechanism for a temperature range of –30 ºC to –5 ºC (Glen, 1955; Homer and Glen, 1978),

655 where both diffusion via grain-boundary, vacancy or interstitial defects (Barnes et al., 1971;

656 Brown and George, 1996; Nasello et al., 2005; Li and Baker, 2022b), and dislocations contribute

657 to the creep of polar firn.

658

659 **4. Conclusions**

660 Constant-load creep tests were performed on three cylindrical specimens tested from depths of 20

661 m (applied stress 0.21 MPa), 40 m (0.32 MPa) and 60 m (0.43 MPa) at temperatures of –5 ±

662 0.2ºC, –18 ± 0.2ºC, and –30 ± 0.2ºC from a firn core extracted at Summit, Greenland in June

663 2017. The microstructures were characterized before and after creep testing using the micro-CT

664 and thin sections viewed between optical crossed polarizers. It was found that:

665

1. Microstructural parameters measured using the micro-CT show that the polar firn densified during the creep compression (e.g. from 685 to 729 kg m^{-3} for the 40 m specimen at -5°C), *viz.*, the TP (from 25.5 to 20.7%), the ECDa (from 0.86 to 0.69 mm), the SSA (from 3.26 to 3.02 mm^{-1}), and the SMI (from -1.85 to -2.8) decreased, while the S.Th (from 0.95 to 0.99 mm) and the CP (from 0.01 to 0.02%) increased. Anomalies in the microstructures, especially at low temperatures of -18°C and -30°C, are likely due to metamorphism under temperature gradients, the radial dilation effect during firn deformation, the measurement uncertainty of the micro-CT, or the anisotropy and the heterogeneity of natural firn.

2. The transient creep behavior of firn at constant stress and different temperatures obeys an Andrade-like law, but, the time exponent k of 0.34–0.69 is greater than the 0.33 found for ice. This is due to fewer grain-boundary constraints in porous firn than in ice.

3. The secondary creep behavior of firn at constant stress and different temperatures presented here shows that the strain at the SRmin increases with decreasing firn density and increasing creep temperature. In particular, low-density firn during creep at high temperatures shows that the strain at the SRmin, e.g. 11.8% and 7.5% respectively from the 20 m and 40 m specimens at -5°C, is greater than the strain of 3%, which is the maximum found at the SRMin of ice.

4. The tertiary creep behavior of firn at constant stress and different temperatures is more easily observed from lower-density specimens at greater effective stresses and higher creep temperatures. The strain softening in tertiary creep is primarily due to recrystallization.

5. The apparent activation energy for the firn creep has a wide range of 61.4–102.8 kJ mol^{-1} because the grains in firn slide more easily along more directions in the more porous and heterogeneous structure, the enhanced fluidity from inclusions, and the topological structure

688   of the firn. In addition, the SRmin is a function of the temperature, depending on the

689   microstructure of firn and the inclusion content. The predicted SRmin increases with

690   increasing firn density at a given temperature and is independent of the effective stress. Lastly,

691   there is no significant difference in the creep mechanism at temperatures ranging from $-30^{\circ}C$

692   to $-5^{\circ}C$.

693

694   The creep of polar firn behaves differently from full-density ice, implying that firn densification is

695   an indispensable process in fully understanding the transformation of snowfall to ice in the polar

696   regions. Observed firn deformation indicates that temperature plays a determined role in firn

697   densification. Thereby, it will be helpful to bridge a gap between the firn temperature and the

698   climate of the past for reconstructing paleoclimate. Also, it will be helpful to apply a confining

699   load to investigate the microstructure of the creep of polar firn with smaller initial particle sizes at

700   low temperatures using the micro-CT. Further studies of interest are to investigate the quantitative

701   relationship between the microstructural parameters and the mechanical behavior of polar firn,

702   and when the onset of recrystallization occurs during creep, as well as verify the SRmin predicted

703   by the relationship of SRmin vs. temperature from the firn specimens at more extensive ranges of

704   stresses and temperatures.

Appendix A: Hydrostatic pressure, the applied stress, and the effective stress

The hydrostatic pressure, p, which varies with temperature, along with the cohesion of the ice and the friction angle between snow particles, plays a significant role in determining the apparent activation energy and, consequently, the strength of the ice (Fish, 1991). It was calculated from the overburden pressure of snow, i.e. $p = \bar{\rho}_f g h$, where $\bar{\rho}_f$ is the average firn density above the depth of interest, h, and g is the acceleration of gravity. At Summit, p at the depths of 20 m, 40 m, and 60 m was estimated to be ~0.1 MPa, ~0.22 MPa, and ~0.38 MPa, respectively. Note that the slope of the surface of ice sheets and glaciers at Summit is idealized to be zero, i.e., their surfaces are horizontal. The applied stress, σ, is the applied load divided by the cross-sectional area of a sample. The σ at the depths of 20 m, 40 m, and 60 m were 0.21 MPa, 0.32 MPa, and 0.43 MPa, respectively. The effective stress, $\tilde{\sigma}$, is defined as σ divided by the fraction of ice matrix in firn, see in detail from Li and Baker (2022a). Thereby, $\tilde{\sigma}$ is 0.32 MPa (the mean porosity of 34.9%), 0.43 MPa (24.8%), and 0.5 MPa (14.4%) from the 20–60 m samples, respectively. Note that the stresses were vertically loaded on the sample (parallel to the direction of core axis of the sample) in laboratory tests. Ideally, in order to be analogous to the densification of firn in nature, $\tilde{\sigma}$ for laboratory samples from a given depth should be equal to the p of firn *in situ* at an equivalently same depth at Summit, namely $\tilde{\sigma}/p = 1$. However, in consideration of the laboratory timeframe for experiments (Pimienta and Duval, 1987), the stresses applied in laboratory tests are usually higher with a resulting higher rate of deformation than those *in situ*. Thus, to observe the effect of the stress on the creep of firn with different densities at different depths, we designed the following configuration of the $\tilde{\sigma}/p$ with depth, *viz.*, 0.32 MPa/~0.1 MPa = ~3.2, 0.43 MPa/~0.22 MPa = ~1.95, and 0.5 MPa/~0.38 MPa = ~1.32 for the samples from the depths of 20 m, 40 m,

727 and 60 m, respectively. In this manner, the decrement of $\tilde{\sigma}/p$ with increasing depth represents

728 the decrease of the effective stress with increasing depth. Also, it's important to note that the

729 strain rates achieved during creep experiments in laboratory settings are 6 to 7 times faster than

730 on ice sheets due to the constraints of conducting experiment in reasonable times, which requires

731 higher loads.

732

733 **Appendix B:** Strain rate minimum inferred via two kinds of constraints

734 To improve the reliability of inferred SRmins, two kinds of constraints were applied. First, the

735 SRmins from the -5°C and -18°C samples are calibrated using Glen's law $\dot{\varepsilon}=A\sigma^n$ with n = 4.3

736 (Li and Baker, 2022a). PC1-SRmin, PC2-SRmin, and PC3-SRmin indicate three possibilities of

737 the SRmins that are calculated from the 20 m, 40 m, and 60 m samples via the *only* SRmin

738 observed at a given temperature (Table 2). As an example, for the -5°C samples, there exist three

739 possibilities from three depths. 1) The SRmin observed from the 20 m sample in bold italic font is

740 used to calculate two other SRmins for the 40 m and 60 m samples in the italic font in the column

741 of PC1-SRmin. 2) In the same manner as in scenario 1), the SRmin observed from the 40 m

742 sample is calculated in the column of PC2-SRmin in the bold italic font, and the SRmin observed

743 from the 60 m sample is calculated in the column of PC3-SRmin in the bold italic font. 3) In the

744 same manner as in scenarios 1) and 2), the SRmin is calculated for the -18 °C samples in turn

745 from three depths. Second, the SRMin of the -30°C samples is inferred on the basis of the range

746 of Q_c, i.e., from 44.8 kJ mol^{-1} (upper bound)   to 113 kJ mol^{-1} (lower bound), using the Arrhenius

747 relation.

Data availability

The data supporting the conclusions in this study are available at https://arcticdata.io/catalog.

Author contribution

Y.L. and I.B. designed the experiments and Y.L. carried them out. Y.L. analyzed the data and visualized the relevant results. Y.L. prepared the manuscript with contributions from all co-authors (K.K. and I.B.).

Competing interests

At least one of the (co-)authors is a member of the editorial board of The Cryosphere.

References:

Adolph, A.C.C., Albert, M.R., 2014. Gas diffusivity and permeability through the firn column at Summit, Greenland: measurements and comparison to microstructural properties. T. Cryosph., 8, 319–328, doi:10.5194/tc-8-319- 2014.

Albert, M.R., Shultz, E.F. and Perron, F.E., 2000. Snow and firn permeability at Siple Dome, Antarctica. Ann. Glaciol. 31, 353-356.

Alley, R.B., Clark, P.U., Huybrechts, P., Joughin, I., 2005. Ice-sheet and sea-level changes. Sci. 310(5747), 456-60. doi: 10.1126/science.1114613. PMID: 16239468.

Ambach, W., Eisner, H., 1985. Rheological properties of temperate firn. Polarforschung, Bremerhaven, Alfred Wegener Institute for Polar and Marine Research & Germany Society of Polar Research 55(2), 71–77. hdl:10013/epic.29564.d001.

Anderson, D.L., Benson, C.S., 1963. The densification and diagenesis of snow. In: Kingery, W.D. (Ed.), Ice and Snow. Press, Cambridge, Massachusetts, M.I.T, pp. 391–411.

Arnaud, L., Gay, M., Barnola, J.M., Duval P., 1998. Imaging of firn and bubbly ice in coaxial reflected light: a new technique for the characterization of these porous media. J. Glaciol., 44(147), 326-332.

Ashby, M.F., Duval, P. 1985. The creep of polycrystalline ice. Cold Reg. Sci. Technol., 11 (3), 285-300. doi:10.1016/0165-232X(85)90052-7.

Azuma, N., Higashi, A., 1984. Mechanical properties of Dye 3 Greenland deep ice cores. Ann. Glaciol.

Baker, R.W., Gerberich, W.W., 1979. The effect of crystal size and dispersed-solid inclusions on the activation energy for creep of ice. J. Glaciol., 24(90), 179-194.

790 Barnes, P., Tabor, D., Walker, J.C.F., 1971. The friction and creep of polycrystalline ice. Proc. Roy.

791   Soc. Lond. A (324),127-155.

792 Bartelt, P., Von Moos, M., 2000. Triaxial tests to determine a microstructure-based snow viscosity

793   law. Ann. Glaciol., 31, 457-462.

794 Bindschadler, R., King, M., Alley, R., Anandakrishnan, S., Padman, L., 2003. Tidally controlled

795   stick-slip discharge of a West Antarctic ice stream. Ann. Glaciol., 36, 157–162.

796 Brown, D.E., George, S.M., 1996. Surface and bulk diffusion of $H_2^{18}O$ on single-crystal $H_2^{16}O$ ice

797   multilayers. J. Phys. Chem. 100 (38) 15460–15469.

798 Budd, W.F., Jacka, T.H., 1989. A review of ice rheology for ice sheet modelling. Cold Reg. Sci.

799   Technol. 16(2), 107–144. doi: 10.1016/0165-232X(89)90014-1.

800 Burr, A., Ballot, C., Lhuissier, P., Martinerie, P., Martin, C.L., Philip, A., 2018. Pore morphology

801   of polar firn around closure revealed by X-ray tomography, T. Cryosphy., Copernicus, 12(7),

802   2481-2500. 10.5194/tc-12-2481-2018. hal-01864373.

803 Butkovich, T.R., Landauer, J.K., 1960. Creep of ice at low stresses. U.S. Snow, Ice and

804   Permafrost Research Establishment. Research Report 72.

805 Chandler, D., B. Hubbard, A. Hubbard, T. Murray, Rippin, D., 2008. Optimising ice flow law

806   parameters using borehole deformation measurements and numerical modelling. Geophys.

807   Res. Lett., 35, L12502.

808 Chen, M., Chen, Z.D., 1997. Effective stress laws for multi-porosity media. Appl. Math. Mech.,

809   20(11), 1207–1213.

810 Coleou, C., Lesaffre, B., Brzoska, J.B., Ludwig, W., Boller, E., 2001. Three-dimensional snow

811   images by X-ray microtomography, Ann. Glaciol., 32, 75-81.

812 Colgan, W., et al., 2023. Sixty years of ice form and flow at Camp Century, Greenland. J. Glaciol.,

813   69(276), 919–929.

814 Courville, Z., Horhold, M., Hopkins, M. and Albert, M., 2010. Lattice-Boltzmann modeling of the

815   air permeability of polar firn. J. Geophys. Res., Earth Surface, 115(F4).

816 Coussy, O., 2004. Poromechanics. John Wiley & Sons.

817 Cuffey, K.M., 2006. Manifestations of ice microphysical processes at the scale of whole ice sheets.

818   In: Knight, P. (Ed.), Glacier Science and Environmental Change. Blackwell Publishing, 290–

819   300.

820 Cuffey, K.M., Paterson, W.S.B., 2010. The Physics of Glaciers, 4th edited. Elsevier Inc.

821 Cuffey, K.M., Kavanaugh, J.L., 2011. How nonlinear is the creep deformation of polar ice? A new

822   field assessment. Geol., 39(11), 1027–1030.

823 da Silva, M.R., Schroeder, C., Verbrugge, J.C., 2008. Unsaturated rock mechanics applied to a

824   low-porosity shale. Eng. Geol., 97, 42–52.

825 Durham, W.B., Stern, L.A., 2001. Rheological properties of water ice applications to satellites of

826   the outer planets. Annu. Rev. Earth Planet. Sci. 29(1), 295–330.

827 Duval, P., 1981. Creep and fabrics of polycrystalline ice under shear and compression. J. Glaciol.

828   27, 129–140.

829 Duval, P. Ashby, M.F., Anderman, I., 1983. Rate-controlling processes in the creep of

830   polycrystalline ice. The Journal of Physical Chemistry, 87, 4066-4074.

831 Duval, P., Montagnat, M., 2002. Comment on 'Superplastic deformation of ice: experimental

832   observations' by D. L. Goldsby and D. L. Kohlstedt. J. Geophys. Res.: Solid Earth. 107(B4),

833   ECV 4-1–ECV 4-2. doi: 10.1029/2001JB000946.hal-01698732.

834 Ebinuma, T., Maeno, N., 1987. Particle rearrangement and dislocation creep in a snow

835   densification process. J Phys.(Paris), 48,Colloq. C1, 263–269.

Ehlers, W., 2002. Foundations of multiphasic and porous materials. In Ehlers Wolfgang and Bluhm J eds. Porous Media– Theory, Experiments and Numerical Applications. Berlin: Springer, pp. 3–86.

Eichler, J., 7 others, 2017. Location and distribution of micro-inclusions in the EDML and NEEM ice cores using optical microscopy and in situ Raman spectroscopy. The Cryosphere. 11(3), 1075–1090. doi: 10.5194/tc-11-1075-2017.

Faria, S.H., Weikusat, I., Azuma, N., 2014. The microstructure of polar ice. Part II: state of the art. J. Struct. Geol. 61, 21–49. doi:10.1016/j.jsg.2013.11.003.

Fish, A.M. (1991) Creep and yield model of ice under combined stress. USA Cold Regions Research and Engineering Laboratory, Special Report 91-31.

Flin, F., Brzoska, J.B., Lesaffer, B., Coleou, C., Pieritz, R.A., 2004. Three-dimensional geometric measurements of snow microstructural evolution under isothermal conditions. Ann. Glaciol., 38, 39-44.

Freitag, J., Dobrindt, U., Kipfstuhl, J., 2002. A new method for predicting transport properties of polar firn with respect to gases on the pore-space scale, Ann. Glaciol., 35, 538-544.

Frost, H.J., Ashby, M.F. 1982. Deformation-mechanism maps: the plasticity and creep of metals and ceramics. Oxford: Pergamon Press.

Fujita, S., Hirabayashi, M., Goto-Azuma, K., Dallmayr, R., Satow, K., Zheng, J., Dahl-Jensen, D., 2014. Densification of layered firn of the ice sheet at NEEM, J. Glaciol., 60 (223), 905-921, doi:10.3189/2014JoG14J006.

Gagliardini, O., Meyssonnier, J., 2000. Simulation of the creep of ice with a self-consistent anisotropic approach. Comput. Mech., 25(5), 479-486.

Glen, J.W., 1955. The creep of polycrystalline ice, Proceedings of the Royal Society A, 228(1175),

519-538, doi.10.1098/rspa.1955.0066.

Goldsby, D.L., Kohlstedt, D.L., 1997. Grain boundary sliding in fine-grained ice I. Scr. Mater. 37(9), 1399–1406.

Goldsby, D.L., Kohlstedt, D.L., 2001. Superplastic deformation of ice: experimental observations, J. Geophys. Res., 106(B6), 11017-11030.

Goodman, D.J., Frost, H.J., Ashby, M.F., 1981. The plasticity of polycrystalline ice, Philos. Mag., A43 665–695.

Gow, A.J., 1969. On the rates of growth of grains and crystals in South Polar firn. J. Glaciol., 8(53) 241-252.

Gray, W.G., Schrefler, B.A., 2007. Analysis of the solid stress tensor in multiphase porous media. Int. J. Numer. Anal. Methods Geomech., 31, 541–581.

Gubler, H., 1978. Determination of the mean number of bonds per snow grain and of the dependence of the tensile strength of snow on stereological parameters. J. Glaciol., 20(83),329-341.

Hammonds, K., Baker, I., 2016. The effects of Ca++ on the strength of polycrystalline ice. J. Glaciol. 62,1–9. doi: 10.1017/jog.2016.84.

Hammonds, K., Baker, I., 2018. The effects of H_2SO_4 on the mechanical behavior and microstructural evolution of polycrystalline Ice. J. Geophys. Res.: Solid Earth. 123,1–22. doi: 10.1002/2017JF004335.

Hansen, B.L., Landauer, J.K., 1958. Some results of ice cap drill hole measurements. IASH Publ. 47 (Symposium at Chamonix 1958– Physics of the Movement of the Ice), 313–317.

Hansen, A.C., Brown, R.L., 1988. An internal state variable approach to constitutive theories for granular materials with snow as anexample. Mech. Mater., 7(2),109-119.

882 Higashi, A., Konimua, S., Mae, S., 1965. Plastic yielding in ice single crystals. Jpn. J. Appl. Phys.

883   4, 575-82.

884 Hildebrand, T., Ruegsegger, P. 1997. A new method for the model-independent assessment

885   ofthickness in three-dimensional images. J. Microsc., 185, 67-75.

886 Hobbs, P.V., 1974. Ice Physics, 1st edited. Oxford University Press Inc., New York.

887 Homer, D.R., Glen, J.W., 1978. The creep activation energies of ice. J. Glaciol., 21(85), 429-444.

888 Hooke, R.L., Mellor, M., Budd, W.F., Glen, J.W., Higashi, A., Jacka, T.H., Jones, S.J., Lile, R.C.,

889   Martin, R.T., Meier, M.F., Russell-Head, D.S., Weertman, J., 1980. Mechanical properties of

890   polycrystalline ice: an assessment of current knowledge and priorities for research. Cold Reg.

891   Sci. Technol., 3, 263-275.

892 Hooke, R.L., 1981. Flow law for polycrystalline ice in glaciers: comparison of theoretical

893   predictions, laboratory data, and field measurements. Rev. Geophys. Space Phys., 19(4),

894   664–672.

895 Hooke, R.L., 2005. Principles of Glacier Mechanics. Cambridge: Cambridge University Press.

896 Horhold, M.W., 5 others, 2012. On the impact of impurities on the densification of polar firn.

897   Earth Planet. Sci. Lett. 325–326,93–99. doi: 10.1016/j.epsl.2011.12.022

898 Hutter, K., Johnk, K., 2004. Continuum Methods of Physical Modeling: Continuum Mechanics,

899   Dimensional Analysis, Turbulence. Springer Science & Business Media.

900 Jacka, T.H. 1984. The time and strain required for development of minimum strain rates in ice.

901   Cold Reg. Sci. Technol., 8 (3), 261-268. doi: 10.1016/0165-232X(84)90057-0.

902 Jacka, T.H., Li, J. 1994. The steady state crystal size of deforming ice. *Ann. Glacial.*, 20, 13–18.

903 Jacka, T.H., Li, J., 2000. Flow rates and crystal orientation fabrics in compression of

904   polycrystalline ice at low temperatures and stresses, Physics of Ice Core Records

905   International Symposium on Physics of Ice Core Records. Shikotsukohan, Hokkaido, Japan,

83-102.

Jonas, J.J., Muller, F., 1969. Deformation of ice under high internal shear stresses. Can. J. Earth Sci. 6(4), 963–968. doi: 10.1139/e69-100.

Jumawan, A.B., 1972. An experimental study of self-diffusion in polycrystalline ice. Diss.Abstr. Int. B 32, 5163–5164 (Abstract).

Kamb, B., 1961. The thermodynamic theory of nonhydrostatically stressed solids. J. Geophys. Res. 66, 259–271.

Khalili, N., Geiser, F. Blight, G.E., 2004. Effective stress in un-saturated soils, a review with new evidence. Int. J. Geomech., 4(2), 115–126.

King, R.F., 1952. Dissertation, Cambridge.

Lade, P.V., Boer, R.V., 1997. The concept of effective stress for soil, concrete and rock. Geotech., 47(1), 61–78.

Landauer, J.K., 1958. The creep of snow under combined stress. Transactions of the society of rheology II. 175-194.

Li, J., Jacka, T.H., Budd, W.F., 1996. Deformation rates in combined compression and shear for ice which is initially isotropic and after the development of strong anisotropy. Ann. Glaciol., 23, 247-252.

Li, Y., Baker, I. 2021. Dynamic observations of the densification of polar firn under compression using a micro-computed tomograph, J. Geophys. Res., Earth Surface,126, e2021JF006290. doi:org/10.1029/2021JF006290.

Li, Y. 2022. Critical values of the microstructural parameters at the first critical density of the densification of polar firn. Cold Reg. Sci. Technol., 198(2022), 10355. doi:org/10.1016/j.coldregions.2022.103553.

929   Li, Y., Baker, I. 2022a. Observations of the creep of polar firn. J. Glaciol., 68(268), 269–287.

930   doi.org/10.1017/jog.2021.91.

931   Li, Y., Baker, I. 2022b. Metamorphism observation and model of snow from Summit, Greenland

932   under both positive and negative temperature gradients in a Micro CT, Hydrol. Processes,

933   e14696. doi.10.1002/HYP.14696.

934   Li, Y. 2023a. Are bubbles in ice the potential space for hydrogen storage? Int. J. Hydrogen

935   Energy, 50(D), 575-585. doi.org/10.1016/j.ijhydene.2023.07.273.

936   Li, Y. 2023b. Changes in grain size during the relaxation stage of viscoelastic firn, Philos. Mag.,

937   104(4), 239-259. doi.org/10.1080/14786435.2023.2296656.

938   Li, Y. Fu, C. Keegan, C. et al. 2023. Microstructural characterization of depth hoar and ice-crust

939   layers using a micro-CT, and hypothesis of ice-crust formation under a thunderstorm, Hydrol.

940   Processes, 37(12), e15060. doi.org/10.1002/hyp.15060.

941   Li, Y. 2024a. Hydrogen production via imperfective ice Ih. Int. J. Hydrogen Energy. 100, 727–

942   735.

943   Li, Y. 2024b. Hydrogen storage-learn from the air clathrate hydrate in polar ice sheets.

944   Sustainable Energy Technol. Assess. 72, 104007.

945   Li, Y. 2024c. The improvement of hydrogen storage capacity via bubbles nucleated in ice-like

946   nanotubes, Mater. Today Sustainability, 27, 100856.

947   Liu, K., Sun, R. & Daraio, C. 2022. Growth rules for irregular architected materials with

948   programmable properties. Sci., 377(6609), 975-981.

949   Lundin, J.M., Stevens, C.M., Arthern, R., Buizert, C., Orsi, A., Ligtenberg, S.R., et al. 2017. Firn

950   model intercomparison experiment (FirnMICE). J. Glaciol. 63(239), 401–422.

951   https://doi.org/10.1017/jog.2016.114.

952   Maeno, N., Ebinuma, T., 1983. Pressure sintering of ice and its implication to the densification of

953   snow at polar glaciers and ice sheets. J. Phys. Chem. 87, 4103–4110.

954 Mahajan, P. and R.L. Brown. 1993. A microstructure-based constitutive law for snow. Ann. Glaciol.,18, 287-294.

956 McCarthy, C., Savage, H., Nettles, M., 2017. Temperature dependence of ice-on-rock friction at realistic glacier conditions. J. Glaciol., 63(241), 595–606.

958 Mellor, M., Smith, J.H., 1966. Creep of snow and ice, CRREL Res. Rep. 220.

959 Mellor, M., Testa, R., 1969. Effect of temperature on the creep of ice. J. Glaciol., 8(52), 131-145.

960 Mellor, M., 1975. A review of basic snow mechanics. Int. Assoc. Hydrol. Sci. 114, 251–291.

961 Meussen, B., Mahrenholtz, O., Oerter, H., 1999. Creep of polar firn. Cold Reg. Sci. Technol. 29, 177–200. doi: 10.1016/S0165-232X(99)00018-X

963 Millstein, J.D., Minchew, B.M., Pegler, S.S., 2022. Ice viscosity is more sensitive to stress than commonly assumed. Commun. Earth Environ., 3, 57.

965 Nasello, O.B., Di Prinzio, C.L., Guzman, P.G., 2005. Temperature dependence of "pure" ice grain boundary mobility, Acta Mater., 53(18) 4863-4869, doi: 10.1016/j.actamat.2005.06.022.

967 Nuth, M., Laloui, L., 2008. Effective stress concept in unsaturated soils: clarification and validation of a unified framework. Int. J. Numer. Anal. Methods Geomech., 32, 771–801.

969 Ogunmolasuyi, A., Murdza, A., Baker, I. 2023. The onset of recrystallization in polar firn. Geophys. Res. Lett., 50, e2023GL103435. doi.org/10.1029/2023GL103435.

971 Paterson, W.S.B., Savage, J.C., 1963. Measurements on Athabasca Glacier relating to the flow law of ice. J. Geophys. Res., 68:4537-43.

973 Paterson, W.S.B., 1977. Secondary and tertiary creep of glacier ice as measured by borehole closure rates, Rev. Geophys. Space Phys., 15, 47–55.

975 Perutz, M.F., Seligman, G., 1939. A crystallographic investigation of glacier structure and the mechanism of glacier flow. Proc. Roy. Soc. London A 172, 335–360.

977 Petrenko, V.F., Whitworth, R.W., 1999. Physics of Ice. Oxford: Oxford University Press.

978 Pimienta, P., Duval, P., 1987. Rate controlling processes in the creep of polar glacier ice. Journal
979 de Physique, 48, 243-248.

980 Raymond, C.F., 1973. Inversion of flow measurements for stress and rheological parameters inva
981 valley glacier. J. Glaciol. 12, 19–44.

982 Salamatin, A.N., Lipenkov, V.Y., Barnola, J.M., Hori, A., Duval, P., Hondoh, T. 2009. Snow/firn
983 densification in polar ice sheets. In: Hondoh, T. (Ed.), III. Firn densification, close-off and
984 chronology, 195-222, Hokkaido University Press.

985 Salm, B., 1982. Mechanical properties of snow. Rev. Geophys. Space Phys., 20(N1), 1–19.

986 Scapozza, C., Bartelt, P.A., 2003. The influence of temperature on the small-strain viscous
987 deformation mechanics of snow: a comparison with polycrystalline ice. Ann. Glaciol., 37,
988 90–96.

989 Schleef, S., Lowe, H., Schneebeli, M., 2014. Influence of stress, temperature and crystal
990 morphology on isothermal densification and specific surface area decrease of new snow. T.
991 Cryosphy., 8, 1825-1838.

992 Sinha, N.K., 1978. Short-term rheology of polycrystalline ice. J. Glaciol., 21(85) 457-472.

993 Steinemann, S., 1954. Flow and recrystallisation of ice. Proc. Int. Assoc. Hydrol. Sci. 39, 449–
994 462.

995 Song, M., Baker, I., Cole, D.M., 2005. The effect of particles on dynamic recrystallization and
996 fabric development of granular ice during creep. J. Glaciol. 51(173), 377–382. doi:
997 10.3189/172756505781829287.

998 Song, M., Cole, D.M., Baker, I., 2006a. Investigation of Newtonian creep in polycrystalline ice.
999 Philos. Mag. Lett. 86(12), 763–771. doi: 10.1080/09500830601023787.

1000 Song, M., Cole, D.M., Baker, I. 2006b. An investigation of the effects of particles on creep of
1001 polycrystalline ice. Scr. Mater. 55, 91–94. doi: 10.1016/j.scriptamat.2006.03.029.

Song, M., Baker, I., Cole, D.M., 2008. The effect of particles on creep rate and microstructures of granular ice. J. Glaciol. 54(186), 533–537. doi: doi:10.3189/002214308785836959.

Srivastava, P.K., Mahajan, P., Satyawali, P.K., 2010. A constitutive law for the densification of polar firn. Cold Reg. Sci. Technol., 60(2), 133-138.

Theile, T., Lowe, H., Theile, T.C., Schneebeli, M., 2011. Simulating creep of snow based on microstructure and the anisotropic deformation of ice. Acta Mater. 59, 7104–7113. doi: 10.1016/j.actamat.2011.07.065.

Thomas, R.H., MacAyeal, D.R., Bentley, C.R., Clapp, J.L., 1980. The creep of ice, geothermal heat flow, and Roosevelt Island, Antarctica. J. Glaciol. 25, 47–60.

Treverrow, A., Budd, W.F., Jacka, T.H., Warner, R.C., 2012. The tertiary creep of polycrystalline ice: experimental evidence for stress-dependent levels of strain-rate enhancement. J. Glaciol. 58(208), 301–314. doi: 10.3189/2012JoG11J149.

Vickers, W., Greenfield, P., 1968. The high temperature creep properties of compacted magnesium powder. *Journal of Nuclear Materials,* 27(1), 73-79.

Wang, X., Baker, I., 2013. Observation of the Microstructural Evolution of Snow under Uniaxial Compression using X-ray Computed Micro-tomography, J. Geophys. Res., 118, 1-12, doi.org/10.1002/2013JD020352.

Weertman, J., 1983. Creep deformation of ice. Annual Review Earth Planet Science, 11, 215–240.

Weertman, J., 1985. Unsolved problems of creep. Nat. 314(6008), 227.

Wiese, M., Schneebeli, M., 2017. Snowbreeder 5: a Micro-CT device for measuring the snow-microstructure evolution under the simultaneous influence of a temperature gradient and compaction. J. Glaciol., 63(238), 355–360, doi: 10.1017/jog.2016.143.